Functional connectivity with short-term dynamics explains diverse patterns of excitatory spike transmission *in vivo*

Abed Ghanbari[1], Naixin Ren[2], Christian Keine[3], Carl Stoelzel[2], Bernhard Englitz[4], Harvey A. Swadlow[2], and Ian H. Stevenson[1,2]

[1] *University of Connecticut, Department of Biomedical Engineering*
[2] *University of Connecticut, Department of Psychological Sciences*
[3] *Carver College of Medicine, Iowa Neuroscience Institute, Department of Anatomy and Cell Biology, University of Iowa*
[4] *Radboud University, Donders Institute for Brain, Cognition and Behavior, Department of Neurophysiology*

Abstract

Fast information transmission in neural networks is heavily influenced by short-term synaptic plasticity (STP), and the type and timescale of STP varies by cell-type and brain region. Although STP has been widely characterized *in vitro* from recordings of postsynaptic potentials or currents, characterizing STP in *in vivo* in behaving animals is difficult due to the lack of large-scale intracellular recordings. Here, we use paired extracellular observations to estimate the short-term dynamics of synaptic transmission from spikes alone. We introduce an augmented generalized linear model (GLM) that includes a dynamic functional connection as well as several, non-synaptic factors that alter spike transmission probability. Our model captures the diverse short-term dynamics of *in vivo* spike transmission at identified synapses and accurately captures the effects of local pre- and postsynaptic spike patterns. We applied this model to large-scale multi-electrode recordings to describe stimulus-dependent shifts in spike transmission and cell-type specific differences in STP.

Introduction

Neural information processing is largely governed by synapses and their dynamics [1,2]. Short-term synaptic plasticity (STP) alters synaptic transmission on timescales from a few milliseconds to several seconds depending on the sequence of presynaptic spiking. Presynaptic STP arises from a mixture of two main processes: depletion of neurotransmitter-containing vesicles, which causes depression, and the elevation of residual Ca^{2+} in the presynaptic terminal, which causes facilitation by increasing vesicle release probability [3]. This can be observed in intracellular recordings where, following repetitive stimulation of the presynaptic terminal, the amplitudes of postsynaptic potentials (PSPs) or currents (PSCs) will either decrease (depression) or increase (facilitation) [3,4]. The degree of STP differs depending on the pre- and postsynaptic cell type [5] and brain region [6,7]. Functionally, STP can act as a temporal filter [8], can allow neural circuits to specialize for specific tasks [9,10], and may also underlie gain control [11], network stability [12], and long-term synaptic plasticity [13]. Here we focus on understanding how STP-induced changes

in PSP/PSC amplitudes shape postsynaptic spiking. *In vivo* studies have shown that postsynaptic spiking probability, similar to the amplitude of PSP/PSCs, depends on the recent history of presynaptic spiking [14,15]. Just as PSP/PSCs show diverse patterns of depression and facilitation, the postsynaptic spiking probability also appears to have complex patterns depending on the brain region and cell-types [16]. However, postsynaptic spiking probability is modified by many additional variables besides STP at a single synaptic input. Here we aim to understand how the pattern of presynaptic spiking activity and short-term synaptic plasticity shape postsynaptic spiking probability.

To do so, we use simultaneously recorded pre- and postsynaptic spiking activity to detect and study putative monosynaptic connections. When an excitatory, monosynaptic connection is present, cross-correlations between the spiking of a pre- and postsynaptic neuron often show a rapid, transient increase in postsynaptic spikes following the presynaptic spike. This occurs at an interval reflecting the presynaptic axonal conduction time plus the synaptic delay (usually < 4 ms) [17,18]. However, this cross-correlation is not static. Previous studies have found that the cross-correlation often differs for presynaptic spikes that are part of a burst compared to isolated spikes [14]. Spike transmission probability appears to depend on the timing of previous presynaptic spikes, and one factor influencing spike probability may be STP [19,20]. For example, depressing synapses would have more reliable synaptic transmission in response to isolated presynaptic spikes following long inter-spike intervals (ISIs) compared to shorter intervals (in bursts) [14,16]. On the other hand, facilitating synapses would show a stronger response to presynaptic spikes following shorter ISIs (bursts) compared to the presynaptic spikes following longer ISIs (isolated) [21]. By looking at the corresponding cross-correlograms from a subset of presynaptic spikes with specific ISIs, previous studies have found highly diverse, non-monotonic spike transmission patterns for different synapses [16]. This diversity in patterns of spike transmission probability, however, is not solely attributable to STP. When two presynaptic spikes occur in close succession, the membrane time-constant may cause postsynaptic potentials (PSP) to sum and increase the spike probability even if the individual PSPs were sub-threshold [22]. Moreover, the history of postsynaptic spiking also affects spike probability such that even if the PSP is strong, it may not trigger a spike if it falls within the refractory period or during an after-hyperpolarization (I_{AHP}) current [23]. Finally, slow fluctuations in the overall excitability of the postsynaptic neuron, due to neuro-modulation, for instance, could also change synaptic transmission probability [24]. In different synapses the degree that each factor contributes varies and leads to diverse patterns of postsynaptic spike transmission probability.

The overall correlation structure in spiking data can often be estimated by generalized linear models (GLMs) [25,26]. However, previous models have treated these interactions as static, and, thus, cannot capture dynamic changes in spike transmission probability. Here we extend these GLMs to describe dynamic interactions between neurons and account for the diversity of spike transmission patterns [26–28]. For each individual presynaptic spike, our model aims to predict postsynaptic spikes accounting for the postsynaptic neuron's baseline firing rate, slow fluctuations

of the postsynaptic firing rate, the effect of postsynaptic spiking history, and a coupling term affected by synaptic summation and short-term synaptic plasticity. The conditional intensity of our model provides estimates of postsynaptic spiking probability following every single presynaptic event based on the previously observed sequence of pre- and postsynaptic spiking. The split cross-correlogram only describes the average response conditioned on the ISI preceding the most recent presynaptic spike. By using a model-based approach we can incorporate the full sequence of presynaptic spikes beyond the most recent one, explicitly account for factors such as postsynaptic history, and link the observed patterns of spike transmission to the underlying dynamics of vesicle depletion and release probability.

To evaluate the model, we first examined its ability to capture the observed patterns of spike transmission probability for three well-studied, strong putative synapses using pre- and postsynaptic spike observations from: 1) a pair of neurons in the mouse thalamus, 2) an auditory nerve projection onto a spherical bushy cell (ANF-SBC) in the gerbil, and 3) a neuron in ventrobasal (VB) thalamus of the rabbit projecting to a putative fast-spike inhibitory neuron in primary somatosensory (S1) barrel cortex (VB – Barrel). Short-term synaptic dynamics of this latter system have been extensively characterized *in vivo* [14,29,30]. Similarly, ANF-SBC synapses have been extensively studied in previous experiments and are well-characterized *in vitro* [31–33]. Using the auditory brainstem connection, we explore how synaptic transmission probability changes depending on the stimulus. Our result suggests that a simplified model, without considering short-term plasticity, is insufficient to explain how patterns of spike transmission change as the pattern of presynaptic input changes. Finally, we apply our model to spiking data from a large-scale, multi-electrode array recorded from multiple areas in an awake mouse. Here we investigate the STP dynamics in putative synapses from excitatory neurons onto two putative inhibitory subtypes (e.g. FS: fast-spiking, RS: regular-spiking). We find that these two types of connections have distinct patterns of spike transmission, where excitatory-FS connections appear to be slightly more depressing than excitatory-RS connections. Together, these results illustrate the diversity of spike transmission patterns *in vivo* and present one potential approach to studying short-term synaptic dynamics in behaving animals.

Most previous approaches to describing interactions between neurons using spiking activity have focused on static functional connectivity. These models improve both encoding and decoding accuracy and have been shown to capture physiological network structure in some cases [34]. Here we model dynamic functional connectivity where the effect of each presynaptic spike on the probability of postsynaptic spiking depends on the previously observed sequence of presynaptic spiking. This augmented GLM can be directly compared with the observed spike transmission probability and also allows us to disentangle the contributions of short-term synaptic plasticity, synaptic summation, presynaptic firing rate fluctuations, and spike history. Moreover, we find that modeling dynamic functional connections allows us to better predict postsynaptic responses compared to the static models. Since modeling static functional connectivity can improve decoding [25,26,35], modeling dynamic functional connectivity may improve decoding further as well. As

multi-electrode arrays improve, and the number of simultaneously recorded neurons increases, models of dynamic functional connectivity may provide insight into not just network structure, but also the extent of depression or facilitation in these networks, as well as differences in network dynamics across multiple brain areas and under different behavioral conditions. Here, our findings suggest that, at least in some cases, *in vivo* spike transmission dynamics differ substantially for different stimuli and different cell-types.

Results

Short-term synaptic plasticity directly affects synaptic information processing by altering the amplitude of presynaptic currents [2], but in most neural systems it remains unclear how these presynaptic effects translate to altered postsynaptic spike probability. Postsynaptic spiking is affected by many factors including short-term plasticity, postsynaptic spike history, summation of PSPs, and slow fluctuations in presynaptic firing rate. Here we developed a statistical model that includes each of these factors and allows their effects to be estimated solely using pre- and postsynaptic spiking activity. In this approach, working with spikes rather than PSC/PSPs enables us to understand the short-term changes in synaptic transmission probability *in vivo* where large-scale intracellular recordings have not been achieved.

Spike transmission probability varies strongly as a function of presynaptic ISIs

Here we define spike transmission probability as the probability of postsynaptic spiking in a window shortly after each presynaptic spike. One conventional approach to study spike transmission and changes in transmission probability are cross-correlograms. Cross-correlograms of excitatory monosynaptic connections show a rapid, transient increase in the postsynaptic spiking probability shortly (usually < 4ms, although this depends on the presynaptic axonal conduction delay) after the presynaptic spike [17]. The timing and shape of the cross-correlogram depends on the synaptic delay, the strength of the connection and varies between synapses. However, in the overall cross-correlogram since all presynaptic ISIs are averaged, the dependence of spike transmission probability on the presynaptic ISIs remains hidden (Fig. 1A). To determine the effect of presynaptic ISI on spike transmission probability we can calculate the cross-correlogram for a subset of presynaptic spikes with a specific ISI. and previous studies showed that transmission probabilities can vary for different ISIs within the same synapse [14,16]. Moreover, the short-term dynamics of spike transmission probability can differ for different synapses as a function of presynaptic ISIs. To illustrate this diversity, we examined three strong synapses from three distinct neural systems: (i) a pair of neurons in thalamus in a mouse, (ii) a projection from ventrobasal to somatosensory barrel cortex (VB-Barrel) in a rabbit, and (iii) the auditory nerve fiber to spherical bushy cell projection in a gerbil (ANF-SBC). Although the presynaptic neurons have diverse ISI distributions (Fig. 1B), splitting the spikes into ISI quantiles and calculating the correlogram for each quantile, demonstrates how postsynaptic responses differ following short and long presynaptic ISIs. For the pair of neurons in thalamus, spike transmission has a higher probability at short and long intervals and a lower probability for mid-range ISIs. For VB-Barrel transmission

probability is higher for longer ISIs, while for ANF-SBC the highest transmission probability occurs at intermediate intervals (Fig. 1C).

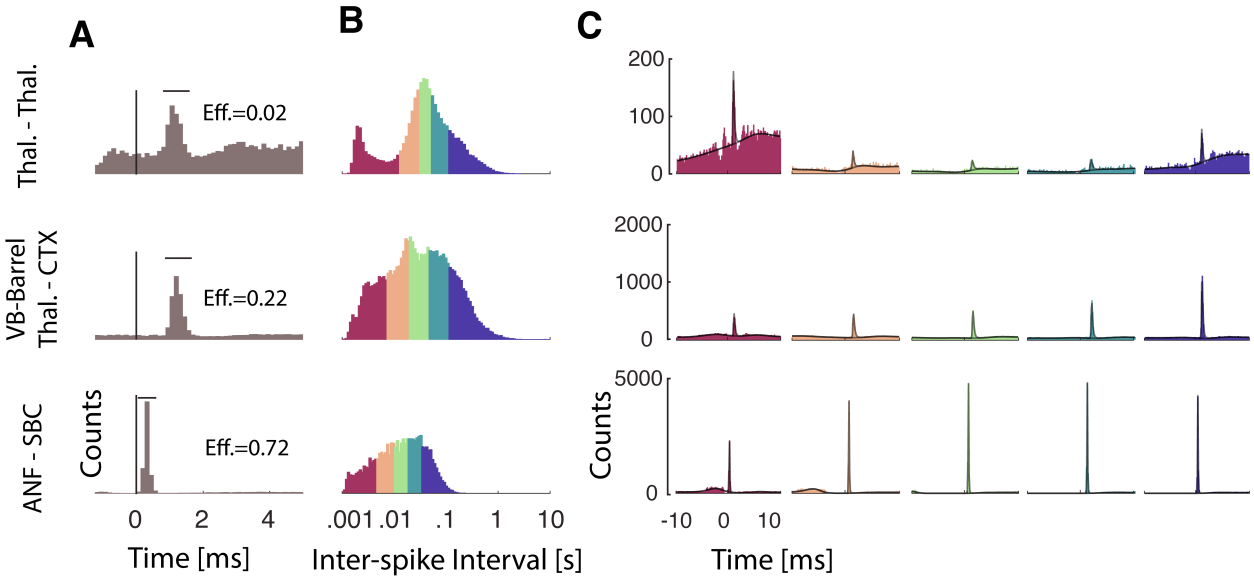

Fig. 1: Spike transmission probability depends on the presynaptic ISI and differs between synapses. A) Cross-correlograms between pre- and postsynaptic spiking show an increase in the postsynaptic spike count (or probability) after a short latency, indicative of a monosynaptic connection. Efficacy (Eff.) for each synapse denotes the ratio between numbers of postsynaptic spikes in the synaptic peak (horizontal bars) corrected for the baseline number of expected postsynaptic spikes to number of presynaptic spikes. **B)** Inter-spike interval distributions (log-scale) for the presynaptic neuron for three different synapses. The distributions are color-coded into 5 quantiles with equal number of presynaptic spikes. **C)** For each ISI quantile, we calculate a separate cross-correlogram. Colors correspond to (B) going from shorter presynaptic ISIs (left) to longer ISIs (right). Note that both the baseline firing rate and the synaptic peak for each connection change as a function of presynaptic ISI. Solid lines overlaying the cross-correlograms illustrate model fits used to estimate the synaptic effect and the smooth baseline.

The shape of spike transmission patterns depends on multiple factors

In synapses exhibiting short-term synaptic plasticity the postsynaptic response after each presynaptic spike changes according to the recent history of presynaptic spiking [28,36]. However, besides synaptic dynamics there are additional factors that alter spike timing. At short presynaptic ISIs, membrane potential summation can lead to larger PSPs and increased spike probability, even in absence of short-term synaptic plasticity [22]. The spiking nonlinearity and the history of postsynaptic spiking can also alter how a given pattern of presynaptic input is transformed into postsynaptic spiking [26,37].

To illustrate how STP, synaptic summation, and postsynaptic history interact to create the observed spike transmission pattern we simulated from a simplified rate model with linear voltage summation, short-term plasticity, a soft spiking nonlinearity, and an after-hyperpolarization (Fig.

2). Similar to experimental data, the spike transmission probability in this simplified model depends on the presynaptic ISI as well as the type of STP. For depressing synapses, the spike transmission probability increases for longer presynaptic ISIs while for facilitating synapses it increases for mid-range ISIs [28,36]. Independent of STP type, PSPs sum at short ISIs (Fig. 2A). However, the exact shape of transmission probabilities also depends on the strength of the synapse and, possibly, the history of postsynaptic spiking. An after-hyperpolarization current following each postsynaptic spike, for instance, can briefly decreases the probability of subsequent spikes. In our simulation, we find that "spike interference" from previous postsynaptic activity can counteract membrane potential summation (Fig. 2B). This type of postsynaptic spike interference generally decreases the spike probability for shorter presynaptic ISIs, but the magnitude of this decrease depends on the synaptic strength and type of STP (Fig. 2C). These simulations illustrate how the pattern of spike transmission probability results from the complex interaction between the membrane potential, the spike nonlinearity, the post-spike history, and short-term synaptic plasticity.

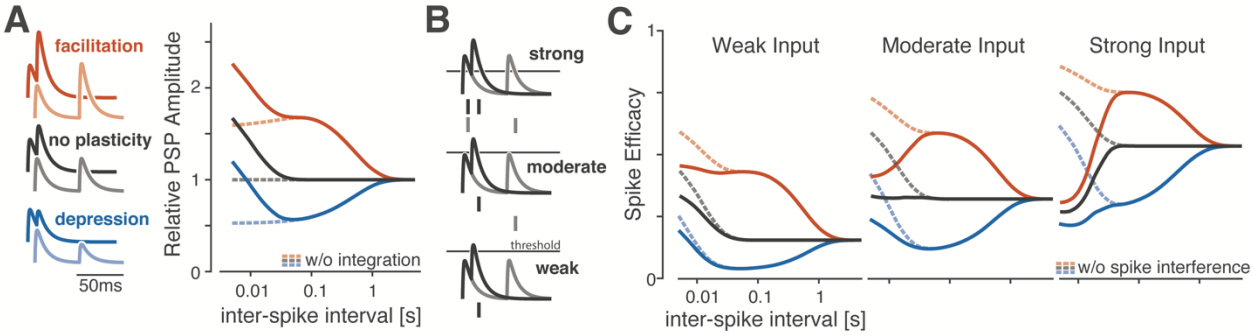

Fig. 2: A simulation of a simplified rate model shows how spike transmission probability depends on multiple factors. A: For different types of short-term synaptic plasticity, postsynaptic summation increases the amplitudes of the postsynaptic potentials (PSP) at shorter ISIs. Lines denote the membrane potential of a postsynaptic neuron in a simplified model as it responds to short (dark traces) and long (light) paired presynaptic pulses. Relative amplitudes of excitatory postsynaptic potentials increase under the simplified model depending on the type of STP (right panel). **B:** Spike generation changes with synaptic strength. In this paired-pulse stimulation paradigm, stronger synapses are more likely to generate a spike following the first presynaptic impulse which can then decrease the spiking probability following the second impulse if there are post-spike history effects. As in (B) traces denote postsynaptic membrane potential responses to short (dark) and long (light) presynaptic ISIs. Dashes denote example postsynaptic spiking, with "spike interference" occurring for strong synapses and short ISIs. **C:** The pattern of spike transmission probability under the simplified model changes depending on the type of STP, the coupling strength, and presence of post-spike interference. Dashed lines show transmission probability without interference from previous postsynaptic spikes, while solid lines show how post-spike history effects can decrease the spike transmission probability.

Spike transmission patterns are diverse across regions and species

The combination of these factors could be one explanation for to the diversity of spike transmission patterns in experimental data. To account for STP, postsynaptic history effects, and slow changes of firing rate we extend a previously developed GLM framework for static functional connections [26] to include short-term dynamics. In the previous, static GLM the probability of postsynaptic spiking is modeled as a linear combination of a baseline firing rate parameter, a post-spike history filter to capture the postsynaptic spike dynamics, such as refractoriness and burstiness, and a coupling filter describing the fixed influence of presynaptic spikes. The sum of these effects is then passed through a spiking non-linearity [26]. In our extended model we added a linear term that allows changes in excitability of the postsynaptic neuron as a function of the presynaptic firing rate (timescale >1min) and allow the coupling term to change for each presynaptic spike according to the Tsodyks and Markram (TM) model of STP [36]. We fit the parameters of this TM-GLM using only the pre- and postsynaptic spike observations and obtain parameters for each effect using approximate maximum likelihood estimation (see Methods). This provides estimates of the history and coupling filters, as in a static GLM, as well as additional parameters for the dynamical synapse (TM model) including facilitation, depression, membrane time constants, and release probability. Given these parameters, the model estimates the postsynaptic spiking probabilities following each observed presynaptic spike and predicts spike transmission probabilities in response to arbitrary patterns of presynaptic inputs.

After fitting the model to real pre- and postsynaptic spike-trains, we compared its behavior to experimentally observed patterns of spike transmission probability. In particular, we compare peaks in the split cross-correlograms to the average model prediction for the same sets of presynaptic spikes (see Methods). We find that our model is flexible enough to explain the changes in synaptic transmission probability observed in spiking statistics for all three synapses above (Fig. 3A). Moreover, using the model-based approach, the contributions of each model component can be disentangled. Our results suggest that the pattern of spike transmission probability for the thalamus connection is dominated by a combination of membrane potential summation and short-term depression. Although depression decreases spike transmission probability at shorter ISIs, membrane summation acts to increase postsynaptic spiking. The ANF-SBC synapse, in contrast, shows an increase in spike transmission probability for a medium range of ISIs that is explained by a model dominated by short-term facilitation. Lastly, the VB-Barrel connection shows a higher postsynaptic response for spikes following longer ISIs (isolated) that is explained by the model as an effect of short-term synaptic depression.

In addition to separating the factors affecting spike transmission, the model also improves the prediction of postsynaptic spike timing. To evaluate how spike prediction accuracy is influenced by STP, we compare the prediction of postsynaptic spiking activity after each presynaptic spike for our model with a static model containing all components except STP. In all three datasets, a model with short-term synaptic plasticity provides substantially better predictions of the postsynaptic spiking activity, assessed by Receiver Operating Characteristics (ROC) curves. For

the model with short-term synaptic plasticity accuracies were AUC=0.76, 0.70, and 0.79 for the Thalamus pair, VB-Barrel, and ANF-SBC connections, respectively; compared to a model without STP where the model accuracies were AUC=0.54, 0.48, and 0.56.

In our model, STP is described by two coupled differential equations with five parameters: $\theta_{stp} = \{\tau_d, \tau_f, U, f, \tau_s\}$ (see Methods). Here we estimate values for depression, facilitation, and membrane time-constants along with release probability, U, and magnitude of facilitation, f, (Fig. 3B). Our result for the thalamus pair shows a higher release probability and depression time-constant with a larger membrane time constant. The VB-Barrel connection shows a higher depression compared to facilitation time constant with a lower membrane time constant. The ANF-SBC synapse shows a lower release probability compared to the other two connections and a lower depression and membrane time constant. Although here we estimate these parameters from pre- and postsynaptic spiking alone, they could also be estimated from intracellular measurements [38]. We are not aware of any *in vivo* experiments that measured depression or facilitation time-constants for these systems. However, previous *in vitro* studies found a wide range of paired-pulse ratios (0.3 to 0.9) in thalamocortical projections [39], consistent with the depressing VB-Barrel synapse here. Additionally, *in vitro* observations of ANF-SBC connections report depression time-constants on the order of 2-25ms in response to a 100 Hz stimulus train [40,41]. These previous estimates are substantially faster than the time-constants estimated by the TM-GLM for the ANF-SBC connection here. However, as mentioned in [40], different patterns of presynaptic input (e.g. regular, Poisson, natural) can result in different time constants, which makes it difficult to compare *in vitro* and *in vivo* STP parameters directly. One parameter that may be more readily comparable across preparations is the membrane time-constant. We find that the estimated membrane time-constant from the TM-GLM for the thalamus pair is consistent with thalamus relay cells observed intracellularly (12.2 $\pm$ 1.1 ms (n=8)) [42], and the estimated membrane time-constant for ANF-SBC is approximately consistent with *in vitro* measurements (1.05 $\pm$ 0.09 ms) [40], as well.

Previous work modeling intracellular recordings suggests that the full TM model may not be necessary to explain STP at some, purely depressing synapses [38]. Therefore, we explored how simplified TM models of STP, with fewer parameters, compare with the full model using the Akaike information criterion (AIC; see Methods). AIC evaluates model accuracy (log-likelihood) penalized by the number of parameters and determines if a simplified model with fewer parameters is preferred over a more complex model. We compare the full model to five reduced models: 1) a model with only integration, without dynamic release probability and resources ($\tau_d, \tau_f = 0$ and $f, U = 1$), 2) a facilitation only model ($\tau_d = 0$), 3) a depression only model ($\tau_f = 0$), 4) a 3-parameter TM model where the magnitude of facilitation is fixed ($f = U$), and 5) a full TM model without resetting integration when a postsynaptic spike occurs ($\pi_i = 1$). For the thalamus pair and VB-Barrel, a model with fixed magnitude of facilitation ($f = U$) performs better while for the ANF-SBC connection the full model gives a better prediction. The full TM model performs well

in all cases, but, for some synapses, as previous results suggested [38], there may be ambiguity with parameter identifiability where many parameter settings explain the data.

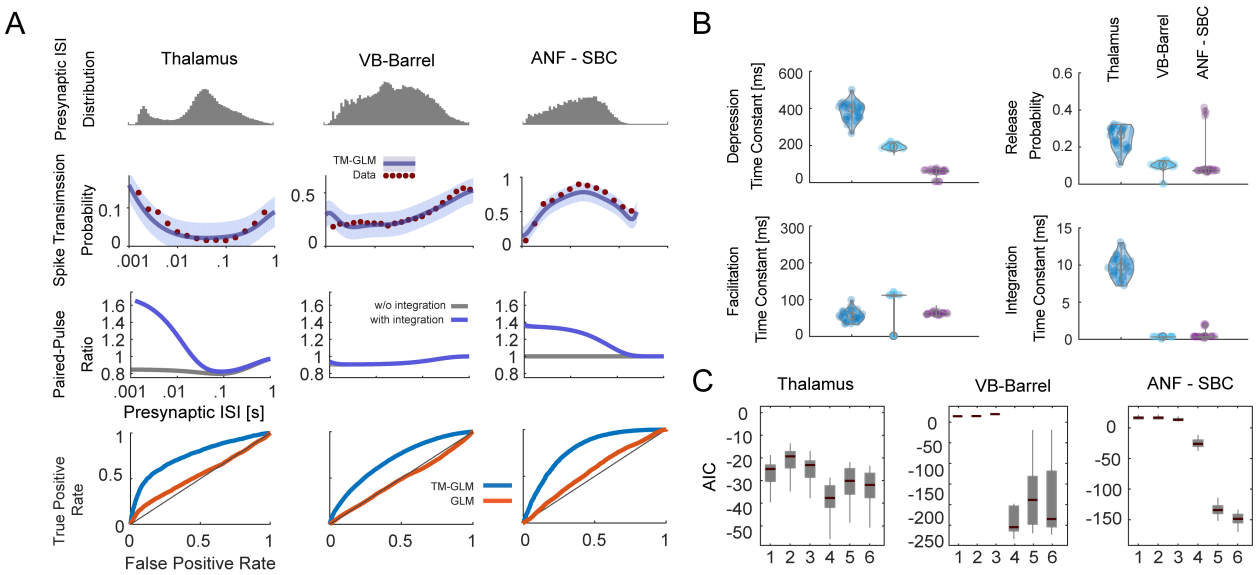

Fig. 3: Model predictions of spike transmission dynamics. A: Spike transmission patterns are diverse across different connections. For three different connections (a pair in thalamus, ventrobasal thalamus to somatosensory cortex, auditory nerve fiber to spherical bushy cell) transmission patterns are explained by a combination of different factors. For each synapse, top panels show the presynaptic ISI distributions (log-spaced). In the second row, the observed spike transmission probability (red data points) and model predictions (blue with 95% confidence bands). We then used the estimated TM parameters for each synapse and simulated responses to for paired presynaptic pulses. Blue curves denote the PPRs of the full model, and gray lines denote PPRs for a model without synaptic summation. In the fourth row, we evaluate how accurately the TM-GLM can prediction individual postsynaptic transmission events. For each individual presynaptic spike, we compare the model transmission probability with the observed binary outcome. ROC curves show the prediction accuracy for the TM-GLM (blue) and a standard GLM without STP (orange). **B:** Estimates for the four STP parameters of the model for each synapse. Each dot represents estimation from a distinct bootstrap sample. **C:** Model comparison for 6 different models (Akaike information criteria relative to a model without plasticity). Models: 1) Integration only ($\tau_d, \tau_f = 0$ and $f, U = 1$), 2) Facilitation only ($\tau_d = 0$), 3) Depression only ($\tau_f = 0$), 4) 3-parameter TM ($f = U$), 5) 4-parameter TM without resetting integration ($\pi_i = 1$), 6) 4-parameter TM.

Recent patterns of pre- and postsynaptic spiking shape the synaptic transmission probability

Although previous studies have focused largely on how spike transmission probability varies as a function of the single preceding presynaptic ISI, synaptic dynamics depend on the full sequence of presynaptic spiking. Unlike *in vitro* experiments where the state of the synapse can, to some

extent, be controlled before studying responses to a specific presynaptic pattern, *in vivo* measurements of spike transmission can be heavily influenced by higher-order correlations between successive ISIs [29]. Additionally, it is difficult to assess the effects of multi-spike patterns empirically by splitting the correlograms, since the number of observations for any given presynaptic spike pattern rapidly decreases with the number of spikes in the pattern. Here we examine how spike transmission depends, not just on the preceding presynaptic ISI, but on triplets of spikes. We compare the empirically observed spike transmission probability following triplets to the estimated spike transmission probability from the TM-GLM. Then, after fitting the TM-GLM, we simulate postsynaptic responses to isolated, local patterns of spikes and determine to what extent the observed spike transmission patterns are influenced by higher-order correlations between successive ISIs.

First, in addition to the timing of the two preceding presynaptic spikes (ISI_1), we split correlograms based on the timing of the three preceding presynaptic spikes using both ISI_1 and ISI_2. Since the TM-GLM provides estimates of the post-synaptic spike probability following every presynaptic spike, we can split both the data and model fits the same way (Fig. 4A). We find that the spike transmission patterns clearly depend on the triplet patterns of presynaptic spikes. That is, the spike transmission probability is influenced by both ISI_1 and ISI_2, and their interaction differed between synapses, as expected from the TM-GLM model. However, similar to the descriptions of spike transmission as a function of ISI_1, the TM-GLM accurately captures the patterns of spike transmission for triplets of presynaptic spikes at those three synapses. In the thalamus pair, spike transmission was dominated by ISI_1, and the effect of ISI_2 appears to be weak or, at least, doesn't appear to be monotonic. Spike transmission at the VB-Barrel connection depends strongly on both ISI_1 and ISI_2, with higher spike transmission probability for longer ISI_2, consistent with recovery from depression. Lastly, for the ANF-SBC connection, transmission probabilities decrease for shorter ISI_2, but there also appears to be a strong interaction between ISI_1 and ISI_2, where transmission probability is high for multiple combinations of these two intervals (e.g. intervals of 10ms then 100ms and intervals of 100ms then 10ms both result in high probability transmission).

To examine to what extent the empirical observations of spike transmission are affected by higher-order correlations between successive ISIs, we again use the estimated parameters in the TM-GLM to simulate postsynaptic responses to hypothetical, isolated triplets of presynaptic spikes. In these simulations we fix the post-spike history effect and the excitability in the model to their average values from model fits, and we fix the initial STP state (initial values of R and u in TM model) for the first spike in triplets to the average R and u values from the model fits. In experimental data, the initial state of the pre- and postsynaptic neurons before the triplets occur can wildly differ between different values of ISI_1 and ISI_2. By simulating, we can compare the influence of different triplets (ISI_1 and ISI_2) when the pre- and postsynaptic neurons start at the same state. Here we find that for the thalamus pair, although the empirical data showed no clear effect for ISI_2, the simulated spike transmission probability increases with short ISI_2, consistent with strong synaptic summation. One reason that this effect may be masked in the empirical transmission probabilities

is that post-spike history effects could act to decrease the probability of future postsynaptic spikes. For the VB-Barrel simulations, we find that short ISI_2 decreases transmission probability, consistent with the empirical transmission patterns, although less pronounced. Serial correlations in the sequence of presynaptic spikes (such as long bursts) could act to accentuate the depression in the empirical observations beyond what we see with the simulated responses to isolated triplets. Finally, for the ANF-SBC, although the empirical transmission probability showed decreased transmission for short ISI_2, the simulated responses to isolated patterns have increasing transmission at short ISI_2 (due to synaptic summation). This difference is likely due to the post-spike history effects, which has been fixed for the simulations, but can have a large effect in the experimental data. Since the overall efficacy of this synapse is quite high (>0.7), is likely that a postsynaptic spike follows the first or second presynaptic spike which then influences the response to the third spike.

To better understand the effects of post-spike history, we examined how the postsynaptic spiking history changes the spike transmission patterns with a similar approach. In addition to splitting the correlograms based on ISI_1, we also split based on the previous postsynaptic ISI, ISI_{post} (Fig. 4B). Here, as with the triplets of presynaptic spikes, we find that the spike transmission patterns depend on the triplet patterns of 2 pre- and 1 postsynaptic spike, and the TM-GLM accurately captures the patterns of spike transmission at our three synapses (Fig. 4B). Here, for both thalamus and VB-Barrel pairs, synaptic transmission probability decreases after a long postsynaptic ISI for all values of ISI_1. In contrast, the ANF-SBC connection shows decreased transmission probability at short postsynaptic ISIs.

As with the triplets of presynaptic spikes, we then simulate how these local patterns of 2 pre- and 1 postsynaptic spike change spike transmission probability when the neurons start from the same initial conditions (average values of excitability, post-spike history, R and u). For the thalamus and VB-Barrel pairs, the simulations of isolated, local patterns match the general trends of empirical spike transmission. However, for the VB-Barrel synapse, the effect of ISI_{post} in the empirical transmission patterns is stronger than in the simulations, suggesting that serial correlations in ISIs could again play a role and does decrease transmission probability for isolated patterns. However, as with the responses to triplets of presynaptic spikes, these local patterns alone are insufficient to explain the empirically observed patterns of spike transmission.

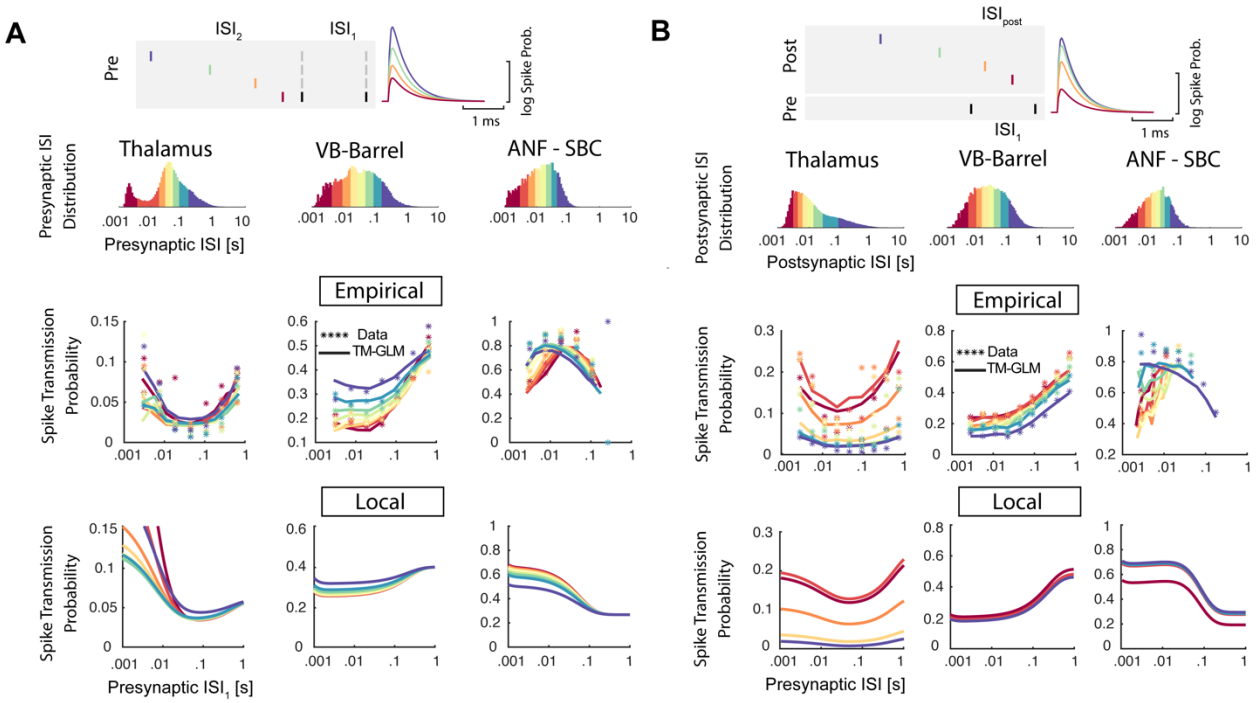

Fig. 4: Effects of pre- and postsynaptic spiking patterns. A: Synaptic transmission patterns change based on the full sequence of presynaptic spiking. Top panel shows a schematic of 4 different patterns of presynaptic spike triplets with a fixed ISI between the two most recent presynaptic spikes (black dashed lines). We split the presynaptic ISI distribution into 8 quantiles. Each data point shows the observed spike transmission probability corresponding to the ISI_2 quantile with the same color. Solid lines are the average estimated probability for each pattern under the model (based on the full sequence of observed spikes). To examine the influence of serial correlations, we then stimulate model responses to the isolated triplet pattern, assuming the synapse is initially in an average state. **B:** Synaptic transmission patterns change depending on the history of postsynaptic spiking, as well. Here each data point in the scatter plots shows the spike transmission probability of the corresponding to the postsynaptic ISIs of the same color in the ISI distribution. Colors represent the corresponding time difference between presynaptic and previous postsynaptic spike. Solid lines are the average predicted probability for quantiles with corresponding colors. Last row shows simulations of the model using estimated STP parameters and fixing the excitability from the model fits to their average values. Here the history effect for each ISI interval is set to the post-spike history filter value on that interval.

Spike transmission patterns change depending on stimulus type

These results suggest that the presynaptic spike pattern has a complex effect on spike transmission probability. In sensory systems, one variable that affects the presynaptic spike pattern is the external stimulus. To examine how differences in stimulus statistics might alter spike transmission, we fitted our model to a dataset recorded juxtacellularly from an ANF-SBC synapse, presented with *natural sounds*, a range of randomized frequency-level pure-tones (*tuning stimuli*), and

403 s*pontaneous activity* in the absence of acoustic stimulation. We merged these three datasets and
404 fitted the model to the merged dataset. As with the previous fits of the ANF-SBC connection (based
405 on a different set of *tuning stimuli*), the transmission probability under all three conditions exhibits
406 a bandpass-like pattern suggesting facilitation and little to no synaptic summation. However, spike
407 transmission during natural stimuli was markedly different from that during pure tone stimulation.
408 During natural sounds, transmission probability is maximized at 100 ms rather than 10 ms in the
409 *tuning stimuli* and during *spontaneous activity*. Further, *natural stimuli* have much lower
410 transmission probability at short ISIs. Interestingly, the TM-GLM captures the overall facilitation,
411 but also captures differences due to the different stimuli. In contrast, a static GLM captures almost
412 none of the variations in spike transmission probability suggesting that a fixed coupling term,
413 postsynaptic history, and, slow fluctuations of presynaptic spiking are not sufficient to capture
414 patterns of spike transmission probabilities (Fig. 5A). Together, these results suggest that the
415 combination of STP, synaptic summation, history, and excitability is sufficient to explain the
416 observed differences between stimuli, without requiring any additional adaptation or plasticity.

417 Since these recordings were performed juxtacellularly, we also have access to the slope of
418 individual (extracellular) PSPs, which correlates with the intracellular PSP amplitude. We
419 compared patterns of individual PSP slopes for each stimulus type and how they correlate with the
420 estimated coupling amplitude following individual presynaptic spikes in our model (Fig. 5B, 5C).
421 Note that patterns of PSP slopes do not have the same pattern as spike transmission probability,
422 since there are other factors (e.g. postsynaptic spiking history) contributing to postsynaptic spiking.
423 These results show the stimulus-dependence of PSP amplitudes and a static GLM without STP
424 cannot account for these variations. Although the correlation is not perfect, the model does
425 correlate with the measured PSP slope, even though the model only has access to spikes. By
426 modeling dynamic functional connectivity, we can approximately reconstruct the amplitude of
427 individual synaptic events.

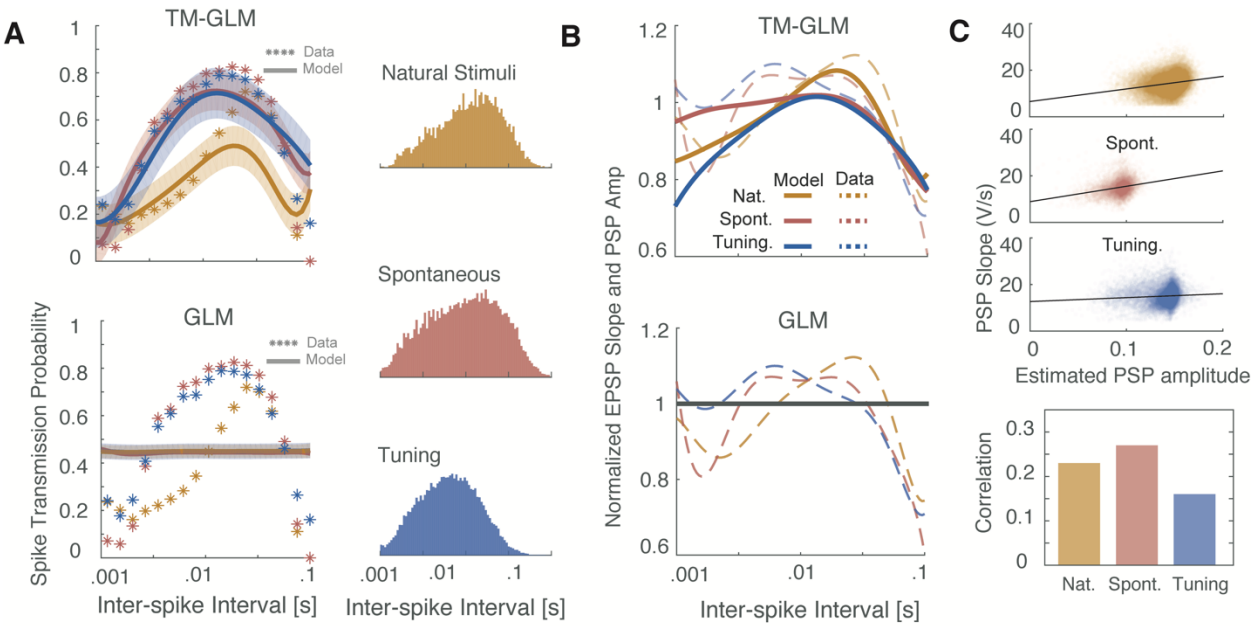

Fig. 5: The TM-GLM captures stimulus-dependent changes in spike transmission probability at the ANF-SBC synapse. A) The TM-GLM captures stimulus-dependent spike transmission probability patterns better than a static model without short-term synaptic plasticity. Asterisks show spike transmission probability for (log-spaced) presynaptic ISIs during two types of auditory stimuli and during spontaneous activity: Natural Sounds (yellow), Spontaneous Activity (red), and Tuning Stimuli (blue). Solid lines and 95% confidence bands show model predictions for each stimulus type. Corresponding inter-spike interval distributions are shown on the right. **B)** The TM-GLM captures changes in extracellularly recorded PSPs. Here the observed PSP slope (dashed lines) approximately matches and coupling term in the TM-GLM (solid lines) for each three stimuli. Although the spike transmission probability of the static GLM can vary as a function of presynaptic ISI due to non-synaptic factors, the coupling term is fixed. **C)** Estimates of individual PSP amplitudes predicted by the model and their PSP slopes in the juxtacellular recording. Black lines denote linear fits and the bar plot shows the corresponding Spearman correlations.

Postsynaptic cell-type specific changes in spike transmission patterns

We applied our model to spiking data from a large-scale multi-electrode array recording to investigate the spike transmission dynamics in synapses from putative excitatory neurons to two different putative inhibitory subtypes. We detected putative synapses using the log-likelihood ratio (LLR < -6, ~200 synapses) between a full model of the correlogram that includes the synaptic effect and smooth model of the correlogram that only captures the slow structure (see Methods). We then found excitatory-inhibitory microcircuits where putative excitatory neurons (based on the cross-correlogram and spike waveform) give inputs to putative inhibitory neurons (41 excitatory synapses onto 9 inhibitory neurons in total). To identify inhibitory neurons as inhibitory, we required the neuron to have an outgoing connection to a third neuron with a fast, transient decrease

in the cross-correlogram. Each of the 9 putative inhibitory neurons here had at least one outgoing connection where the spiking probability of a downstream neuron decreases >18% relative to baseline following its spiking (Fig. 6A and supplementary figures for individual cross-correlograms). We then categorized each neuron as a putative fast-spiking (FS, n=5) or regular-spiking (RS, n=4) unit based on the spike waveform and firing rate (Fig. 6B). Putative FS units had narrow-width spike waveforms (half-width of the trough = .08$\pm$.02 ms) and higher firing rates (26.07$\pm$9.6 Hz) compared to putative RS neurons (n=4) with broader waveforms (half-width = .14$\pm$.02 ms) and lower firing rate (10.18$\pm$10.01 Hz).

We identified these microcircuits in different regions with 4 putative excitatory-inhibitory microcircuits recorded in hippocampus (depth differences: 77.2$\pm$49.4 μm), 3 in thalamus (49.4$\pm$26.2 μm), and 2 in motor cortex (36.4$\pm$23.5 μm). Putative excitatory neurons showed a wide spike waveform (half-width = .18$\pm$.04 ms) similar to the putative regular-spiking inhibitory neurons, but these two classes can be distinguished by their outgoing connection types (e.g. inhibitory/excitatory) [43] (Fig. 6B). Average efficacies from putative excitatory-FS connections (.22$\pm$.12, n=22) were larger, on average, compared to putative excitatory-RS efficacies (.13$\pm$.13, n=19). We then fit the TM-GLM to data from these 41 putative synapses, similar to the three identified synapses above. We find that the STP parameters for these two types of synapses largely overlap, except for the membrane time-constant. Interestingly, the membrane time-constants measured for these inhibitory subtypes *in vitro* overlap with our estimates here (Fig. 6C) [44]. Although *in vitro* studies have not explored the same TM model used here, there is evidence of postsynaptic cell-type specific STP where putative excitatory-RS connections show facilitation and putative excitatory-FS connections show depression [5]. Here we find that both connection types are somewhat facilitating but excitatory-FS connections having a slightly shorter facilitation time constant. However, unlike what would be expected if excitatory-FS connections were depressing, the release probability of excitatory-FS connections is lower than for excitatory-RS connections (Fig. 6C).

To better understand synaptic transmission *in vivo* it is important to consider not just the parameters of the synapse but the full history of presynaptic spiking in the individual presynaptic neurons. We use the estimated model parameters to simulate responses to a train of regular presynaptic spikes with the frequency matched to the average firing rate of the corresponding excitatory input. In simulating postsynaptic responses to the spike train, we fix the excitability and postsynaptic history to their average values from model fits and set the initial STP state of the first spike in the train to the average R and u values from model fits. With these input-matched simulations, excitatory-RS connections show a higher postsynaptic potential compared to excitatory-FS connections (Fig. 6D). Similarly, we simulated the paired-pulse ratio (PPR) at different inter-stimulus intervals in our TM model following the average state. On average, connections to regular-spiking inhibitory neurons show a higher PPR (Fig. 6E). For all connections, we then evaluated the spike prediction accuracy of a model without STP (e.g. static GLM) with our TM-GLM using the Area Under the ROC Curve (Fig. 6F). The model with STP

(TM-GLM) gives more accurate predictions when the postsynaptic neuron spikes following a presynaptic spike for our population of 41 putative excitatory-inhibitory connections (AUC=.69±.05) in comparison with the static GLM (AUC=.50±.03). Altogether, these results illustrate how a dynamic model of functional connectivity, such as the TM-GLM, may allow us to investigate cell-type-specific differences in short-term synaptic dynamics in behaving animals using only pre- and postsynaptic spiking.

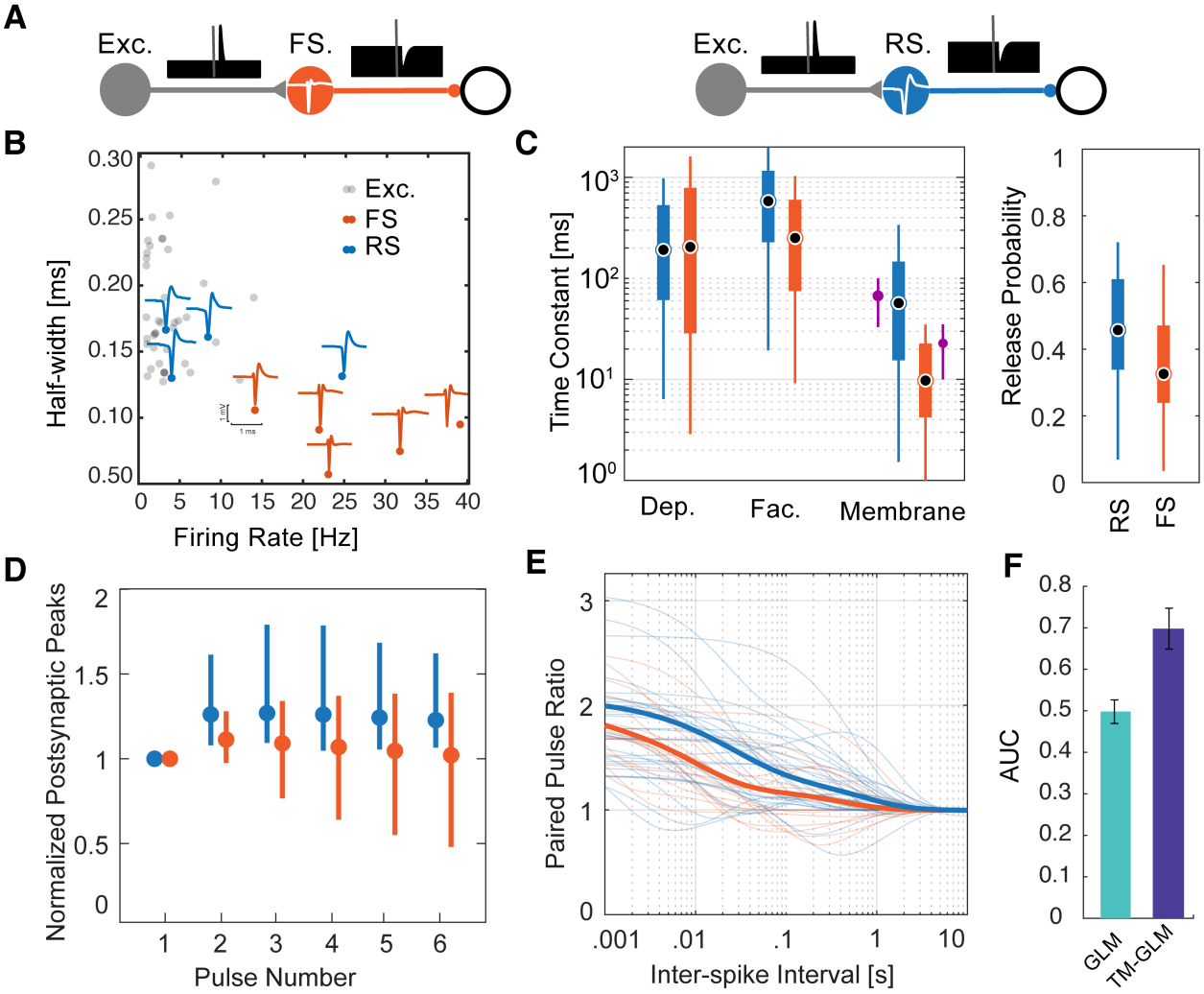

Fig. 6: Distinctive short-term synaptic plasticity dynamics in connections between excitatory neurons to putative Regular-Spiking (RS) and Fast-Spiking (FS) inhibitory neurons. A) Here we examine putative synapses between excitatory neurons and inhibitory neurons (identified by their cross-correlations) and separate the putative inhibitory neurons into two classes: fast-spiking, which have narrow spike waveforms and high rates (left), and regular-spiking (right), which have wide waveforms and lower rates. Identifying these synapses requires both finding both a putative excitatory input and a putative inhibitory output for the same neuron. B) Half-widths (of the trough) of the spike waveforms and firing rates for the FS (orange) and RS (blue) inhibitory

neurons, as well as, their excitatory inputs (grey). Individual blue and orange waveforms (maximum amplitude across the MEA) are shown for all 9 putative inhibitory neurons. C) Estimated depression, facilitation, and membrane time-constants for excitatory-RS and excitatory-FS connections, along with the release probability (right). The purple error-bar next to the membrane time-constant estimations show the median and standard deviations from *in vitro* experiments [44]. D) Simulated postsynaptic potential amplitudes estimated from Tsodyks-Markram model of short-term synaptic plasticity using estimated parameters. For each synapse, PSPs are estimated in response to a pulse train with inter-pulse intervals set to their corresponding average presynaptic inter-spike intervals. Dots and error bars denote the median and inter-quartile range for excitatory-RS (blue) and excitatory-FS (red) connections. E) Simulated Paired-Pulse Ratio for individual synapses of excitatory-RS (blue) and excitatory-FS (red) connections as a function of the presynaptic ISI. F) Area Under the Curve (AUC) of postsynaptic spiking prediction using the static GLM without short-term synaptic plasticity (green) and the TM-GLM with short-term synaptic plasticity (blue).

Discussion

Short-term synaptic plasticity (STP) has been extensively studied *in vitro* and with intracellular recordings where the amplitudes of individual postsynaptic potential/currents (PSP/PSCs) can be directly measured. By using controlled experiments with specific, structured presynaptic spike patterns these studies established how short-term synaptic dynamics can be described by the interactions between release probability and vesicles/resource dynamics [36]. These alterations in PSP/PSP amplitudes can affect the statistics of postsynaptic spiking. Thus, STP could, explain why the probability of postsynaptic spiking depends not just on the presence of a presynaptic spike, but on the timing of the most recent presynaptic inter-spike interval [14,16]. However, the relationship between STP and *in vivo* spike transmission patterns is complex. Patterns of postsynaptic spike transmission are highly diverse and multiple factors beyond STP and the most recent presynaptic ISI shape these patterns. Here we aimed to disentangle the different contributions to spike transmission by developing an augmented generalized linear model, the TM-GLM that explicitly includes STP dynamics as slow changes in postsynaptic excitability and the history of postsynaptic spiking.

Synapses with different types of STP can allow the same sequence of presynaptic spikes to generate different patterns of postsynaptic spiking and thereby control the information flow in the brain. Here we tracked the observed spike transmission probability of three strong synapses from different species and brain areas. The dynamical spike transmission model enables us to disentangle different factors (e.g. slow firing rate changes, postsynaptic spiking history, synaptic summation, and STP) that shape these diverse patterns. First, we investigate the role of STP and the full sequence of presynaptic spiking activity in shaping the spike transmission patterns. In three strong synapses (an intra-thalamic synapse, a thalamocortical synapse, and an auditory brainstem synapse) we show how models of functional connectivity with short-term synaptic plasticity can

1) capture diverse pattern of spike transmission probability, 2) disentangle these transmission patterns to the multiple factors that shape postsynaptic response, 3) extract biologically plausible synaptic dynamics, and 4) improve prediction of postsynaptic spiking.

Estimating static functional connectivity using spike times has revealed network structure in the retina [26] and hippocampus [45], can reconstruct true physiological circuitry [34], and improves encoding and decoding [25,26,35]. However, synaptic weights change over a wide range of timescales depend on external stimuli and behavior [20]. Additionally, synaptic dynamics can shape information transmission in different ways for different pattern of presynaptic spiking, e.g. different behavioral tasks. Although, standard GLMs can partially capture the first-order effects of recent presynaptic spikes on postsynaptic spiking probability, they fail to capture the nonlinear dynamics of synaptic transmission affected by the whole sequence. Here, in a recording from the endbulb of Held (ANF-SBC) we found that spike transmission patterns differed for different stimuli (natural sound stimuli, varying pure tones and without stimulation - e.g. spontaneous activity), and these differences were well-described by the TM-GLM. Although the STP-parameters were the same for all stimuli, the different presynaptic spike patterns yield different synaptic dynamics and different patterns of spike transmission. Since spike transmission probability in the TM-GLM depends on the full history of presynaptic spiking, this model can account for changes on behavioral timescales even in the absence of adaptation or other forms of plasticity (e.g. STDP, LTP).

Cell-type specific interactions in layers and regions of the brain perform different computational tasks. Previous *in vitro* studies have shown that STP dynamics depend on both presynaptic and postsynaptic cell-types [5]. Here in a large multi-electrode array recording of a freely behaving mouse we investigated STP dynamics of synaptic connections from putative excitatory neurons to two different subtypes of putative inhibitory neurons: fast-spiking and regular-spiking. Using inferred short-term dynamics, predicted responses to train of spikes with the same input frequencies as the presynaptic neuron in those connections show facilitation in excitatory-RS and depression in excitatory-FS connections which are in line with previous *in vitro* findings [5]. Moreover, the model with short-term dynamics significantly improves the prediction of postsynaptic activity. As large-scale extracellular recordings advance, models such as the TM-GLM are promising to characterize and compare the short-term dynamics of spike transmission of many different cell types, brain regions, and species.

Although our model provides a tool to characterize the dynamics of spike transmission, there are limitations on how well TM-GLM can capture true synaptic dynamics. Firstly, functional connections inferred from spikes do not necessarily guarantee anatomical connections. A peak in the cross-correlogram does not uniquely indicate the presence of a monosynaptic connection [46,47]. Here we assume that the transient, short-latency increase in postsynaptic spiking activity following a presynaptic spike indicates the presence of an excitatory monosynaptic connection [17]. Nevertheless, verifying connections using optogenetics, juxtacellular recordings [48],

583 imaging [49] or anatomical reconstruction provide a more accurate estimate of true anatomical
584 connections. Secondly, to model short-term dynamics in spiking neurons we employ a rate model
585 that does not explicitly account for the detailed membrane potential of the postsynaptic neuron.
586 Other approaches to modeling synaptic transmission with realistic spike-generation mechanisms,
587 currents, and even dendritic morphology do exist, but are typically less computationally tractable
588 [50]. Here we employed an augmented GLM with a logistic spike nonlinearity. We chose the
589 logistic nonlinearity over the conventional exponential function as it appears to better describe
590 strong connections, such as the ANF-SBC, but other nonlinearities may be better for other neurons
591 [51]. There are also alternatives to the Tsodyks-Markram model for modeling synaptic dynamics.
592 The TM model is biologically plausible, but, since it is deterministic, it ignores the stochasticity
593 of synaptic release and only tracks the dynamics of average postsynaptic potentials. Finally, there
594 are many covariates that could be added to improve model performance, including local field
595 potentials, connections to other simultaneously observed presynaptic neurons [35], higher-order
596 history or coupling terms [52,53], and covariates related to other types of plasticity [52,54–57].
597 Despite these simplifying assumptions and the fact that we only observe a fraction of inputs to the
598 neuron, the TM-GLM captures a wide diversity of *in vivo*, excitatory spike transmission patterns.

599 Short-term synaptic plasticity alters information transmission from presynaptic to postsynaptic
600 neurons by dynamically changing the synaptic efficacy [14,16,36]. Intracellular studies *in vitro* or
601 with artificial stimulation patterns have shown that short-term synaptic dynamics depend on cell-
602 types and brain regions [5,58]. However, there is evidence that, in addition to these anatomical
603 dependencies, short-term synaptic dynamics also depend on stimulus type and the larger
604 computational function of the neural circuit [59]. To understand how these synaptic dynamics alter
605 neural computations we will need to study them during natural patterns of presynaptic spiking [60]
606 and, ultimately, during natural behavior. Since large-scale intracellular recordings are currently
607 not feasible *in vivo*, here we examined the possibility of using existing large-scale extracellular
608 recordings to quantify the dynamics of spike transmission and infer the short-term dynamics of
609 synaptic responses. We find that including STP in models of spiking neurons can capture diverse
610 patterns of spike transmission, including patterns that are stimulus-dependent and cell-type-
611 specific. Additionally, these models substantially improve prediction of postsynaptic spiking
612 following presynaptic spikes and, at least in some cases, can approximately reconstruct individual
613 PSP amplitudes.

614 Material and methods

615 Neural Data

616 To illustrate how synaptic dynamics can be estimated from spikes, we first examined a set of three
617 strong putative or identified synapses with diverse spike transmission probability patterns: (i) a
618 dual-electrode recording of a thalamocortical projection in the barrel system, (ii) an *in vivo* loose-
619 patch (juxtacellular) recording at the calyceal endbulb of Held synapse in the auditory brainstem,
620 and (iii) a recording from a pair of neurons in the thalamus detected from a larger multi-electrode

621 array (MEA) recording. Next, we applied our model more generally to analyze a large sample of
622 putative synaptic connections recorded from the MEA dataset. The data from these three identified
623 strong synapses and the MEA data have been collected from different species, regions, cell-types,
624 under different stimulation and show a diverse pattern of postsynaptic spiking probability. In all
625 cases we deduce short-term synaptic dynamics on the basis of only pre- and postsynaptic spike
626 observations.

627 For the first putative synapse, we use *in vivo* data from simultaneous extracellular recordings in
628 ventrobasal (VB) thalamic barreloids and topographically aligned, somatosensory cortical barrel
629 columns (VB-Barrel) in awake, unanesthetized, adult rabbits. Detailed surgical and physiological
630 methods have been described previously [61]. Spike-triggered averages of the cortical spikes
631 following spiking of the VB neuron was used to identify connected S1 neurons. Based on the
632 presence of high frequency discharge (3+ spikes, > 600 Hz) following electrical stimulation of the
633 thalamus, and narrow spike waveforms, the S1 neuron in this recording was identified as a putative
634 inhibitory neuron [62]. These recordings identified several putative thalamocortical projections.
635 The putative synapse that we model here is particularly clear, with 68,345 pre- and 128,096
636 postsynaptic spikes recorded over the course of 92 minutes of spontaneous activity and has been
637 previously studied in [14,63].

638 For the second synapse, we examined *in vivo* loose-patch recordings at the Endbulb of Held in
639 young adult gerbils. Detailed surgical and physiological methods have been previously described
640 [64]. Briefly, the glass electrode was positioned in the anterior portion of the ventral cochlear
641 nucleus (AVCN) and single-units were recorded during varying acoustic stimulation. Single units
642 were classified when recording a positive action potential amplitude of at least 2 mV and showing
643 the characteristic complex waveform identifying them as large spherical bushy cells (SBC) of the
644 rostral AVCN. This recording included a mixture of juxtacellular waveforms: an isolated
645 excitatory PSP (EPSP) or an EPSP followed by a postsynaptic action potential. For both cases the
646 timing of EPSPs and spikes and rising slope of the EPSPs were extracted. The timing and slope of
647 the EPSPs were identified using a slope threshold for the rising part of EPSPs as previously
648 described [65]. We then modeled spike transmission probability patterns for two recordings: (i)
649 during randomized pure tone acoustic stimulation and (ii) during multiple stimuli, i.e. randomized
650 frequency-level pure tone stimulation interspaced with spontaneous activity, natural sounds, and
651 also during spontaneous activity. Using this second dataset, we characterized how variable
652 presynaptic spike patterns evoked by different stimuli affected the patterns of spike transmission
653 at the same synapse.

654 We also use MEA spiking data to study the factors shaping spike transmission probability patterns
655 in a large-scale recording with multiple cell-types. Here we use a previously collected, publicly
656 available recording from the Cortex Lab at UCL [66,67] with data from two Neuropixels electrode
657 arrays recorded simultaneously, each with 960 sites (384 active) with lengths of 10-mm and
658 spacing of 70 × 20-µm (http://data.cortexlab.net/dualPhase3/). The two electrode arrays span

multiple brain areas and ~90 min of data was collected in an awake, head-fixed mouse on a rotating rubber wheel during visual stimulus presentations. Spikes were automatically detected and sorted using Kilosort [68] on the broadband (0.3–10 kHz) signal and then manually curated. If two clusters of spikes had similar waveforms, cross-correlogram features, and spike amplitudes, they were merged into a single cluster and assigned to a single neuron. In total, 831 well-isolated single neurons where identified from the two probes in several different brain areas: visual cortex (n=74), hippocampus (n=64), thalamus (n=244), motor cortex (n=243), and striatum (n=200). Due to the large number of simultaneously recorded neurons in this dataset, there are many potential synapses (~831^2).

Synapse Detection:

To identify putative monosynaptic connections between well-isolated single neurons, we looked for specific patterns in the cross-correlograms [46]. If two neurons are monosynaptically connected, the probability of postsynaptic spiking increases/decreases rapidly following a presynaptic spike. In spiking data, this rapid, transient change can be seen in cross-correlograms as an asymmetric bump/dip in the number of postsynaptic spikes following presynaptic spikes [18]. For each connection we calculated the cross-correlogram in a 5 ms window before and after presynaptic spikes with bin-size of 0.1 ms. To avoid aliasing in the cross-correlograms, we added a small, random shift to each postsynaptic spike drawn uniformly between $-\Delta t/2$ and $\Delta t/2$ where Δt is the spike time resolution (0.01 ms in most cases). Here we used a model-based approach using the cross-correlograms to decide whether two synapses are monosynaptically connected. To fit the cross-correlogram we used a baseline rate μ, a linear combination of B-spline bases $\boldsymbol{B}(t)$, and a weighted alpha function to model the synapse, $w\,\boldsymbol{\alpha}(t)$, all passed through an output nonlinearity; $\lambda(t) = \exp\big(\mu + \boldsymbol{r}\boldsymbol{B}(t) + w\,\boldsymbol{\alpha}(t)\big)$. The alpha function, $\boldsymbol{\alpha}(t) = (t - t_d)/\tau_\alpha \exp(1 - (t - t_d)/\tau_\alpha)$, describes the shape of the synaptic potential where t_d is the synaptic delay and τ_α is the synaptic time-constant [22]. For individual connections, we estimate these parameters by maximizing the penalized Poisson log-likelihood $l(\mu, \boldsymbol{r}, w, t_d, \tau_\alpha) = \Sigma y_i log\lambda_i - \Sigma\lambda_i + \epsilon\|\boldsymbol{r}\|_2$ where y_i is the number of postsynaptic spikes observed in the i-th bin of the correlogram and $\|\boldsymbol{r}\|_2$ regularizes the model to penalize B-spline bases for capturing sharp increases in the cross-correlogram. ϵ is a regularization hyper-parameter which we set to 1 based on manual search. Due to the parameterization of $\boldsymbol{\alpha}(t)$, the log-likelihood is not concave. However, since the gradient of the log-likelihood can be calculated analytically, we efficiently optimize the likelihood using LBFGS. During the optimization, the delay and time-constant parameters are log-transformed, allowing us to use unconstrained optimization, even though they are strictly positive. We used random restarts to avoid local maxima. To identify putative monosynaptic connections in the large-scale multi-electrode array data, we compared this model with a smooth model with slow changes in cross-correlogram and without the synapse, $\lambda_0(t) = \exp(\mu' + \boldsymbol{r}'\boldsymbol{B}(t))$, using the log-likelihood ratio (LLR) test between our full model with synapse and the nested smooth model. Since low values of the likelihood ratio mean that the observed result was better explained with full model as compared to the smooth model, we then visually screened

pair-wise connections with lowest ratios (LLR < -6) compared to the null model to find putative synapses. Out of ~831^2 possible connections in this dataset we find ~200 putative synapses (0.03%). We handpicked a strong putative synapse between two thalamic neurons to study its efficacy pattern in detail alongside the VB-Barrel and ANF-SBC synapses.

In addition to this single strong synapse, we also categorize putative pre- and postsynaptic cell types for the connections detected in the MEA dataset. For this purpose, we assessed single units based on their cross-correlograms, firing rates, and spike waveforms. We categorized units as excitatory or inhibitory if, in accordance with Dale's law [69], all outgoing cross-correlograms showed transient, short-latency (<4ms) increase/decrease in spiking probability [35]. We then looked into identified inhibitory neurons and categorized them into to putative fast-spiking (FS) and regular-spiking (RS) inhibitory neurons. Using these putative Excitatory-FS and Excitatory-RS synapses, we then examine how the spike transmission patterns differ for these two subtypes of inhibitory neurons.

Extending a Generalized Linear Model to Account for Short-term Plasticity (TM-GLM)

Short-term synaptic plasticity causes the amplitude of postsynaptic potentials (PSP) to vary over time depending on the dynamics of synaptic resources and utilization and can be modeled using the pattern of presynaptic spiking [36,70]. However, changes in the overall postsynaptic spiking probability cannot be uniquely attributed to changes in amplitudes of postsynaptic potentials. To accurately describe the dynamics of spike transmission, we also need to account for the membrane potential summation, the excitability of the postsynaptic neuron (e.g. slow changes in the presynaptic firing rate) and the dynamics of postsynaptic spiking (e.g. refractory period, after hyperpolarization current). We developed an extension of a generalized linear model, which we call a TM-GLM to describe each of these effects. Concretely, the probability of a postsynaptic spike shortly after each presynaptic spike accounts for the full sequence of previous presynaptic spiking and the recent history of postsynaptic spiking. We define the conditional intensity of the postsynaptic neuron after the i-th presynaptic spike, $t_s^{(i)}$, so that the probability of observing a postsynaptic spike in the j-th time bin after the i-th presynaptic spike is given as:

$$\lambda_i(t_j) = \sigma\left(\beta_0 + X_c\left(t_s^{(i)}\right)\beta_c + \sum_{t_r^{(l)} < t_s^{(i)}} X_h\left(t_s^{(i)} - t_r^{(l)}\right)\beta_h \; + \; A_s \, w_i \, \alpha(t_j)\right)$$

where $t_r^{(l)}$ are the postsynaptic spike times preceding $t_s^{(i)}$. For each presynaptic spike, our model decomposes the firing rate of the postsynaptic neuron into four effects: a baseline firing rate, β_0, slow fluctuations in presynaptic firing rate $X_c\beta_c$, history effects from the recent postsynaptic spikes (prior to $t_s^{(i)}$), $X_h\beta_h$, and a time-varying coupling effect from the presynaptic input, $A_s w \, \alpha(t)$ (Fig. 7).

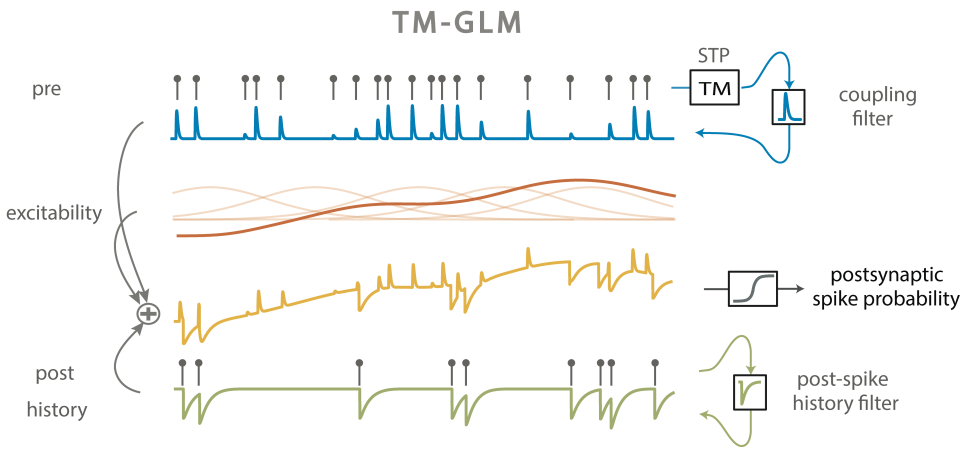

Fig. 7: TM-GLM. Postsynaptic spiking probability before passing the spiking nonlinearity (yellow) changes as a linear combination of presynaptic coupling term with STP dynamics (blue), postsynaptic spiking history (green), the postsynaptic excitability (red). Transparent red curves show the bases of slow changes in postsynaptic probability at presynaptic spike times (X_c).

Here we model slow fluctuations in the postsynaptic rate $X_c\beta_c$ with a linear combination of B-splines with equally spaced knots every 50 seconds of recording time. In the history term, splines (X_h) span a period of 10 ms prior to each presynaptic spike with 4 logarithmically-spaced knots. By scaling $\boldsymbol{\alpha}(t_j)$ with a multiplicative factor, w_i, the strength of a synapse can vary over time and, in this case, depends on the detailed sequence of presynaptic spiking and their corresponding inter-spike intervals. A_s is the magnitude of the synaptic strength. In this case we use a model for short-term synaptic plasticity that allows both depression (where the w_i decreases for shorter presynaptic ISIs) and facilitation (where the w_i increases for shorter presynaptic ISIs), and incorporates membrane summation. To model these effects, w_i is determined by a nonlinear dynamical system based on the Tsodyks and Markram (TM) model [36,71] where: $w_i = w_{i-1}\ \exp\left(-\frac{t_s^{(i)}-t_s^{(i-1)}}{\tau_s}\right)\pi_i + R_i u_i$, where τ_s is the membrane time-constant and the first term of the equation describes how postsynaptic membrane potential summation increases the probability of postsynaptic spiking. This membrane summation will be ignored if there is a postsynaptic spike: $\pi_i = \left\{0 \text{ if } t_s^{(i-1)} < t_r^{(i-1)} < t_s^{(i)}; 1 \text{ otherwise}\right\}$. In the second term of this equation, R represents the dynamics of resources and u describes their utilization.

$$R_i = 1 - [1 - R_{i-1}(1 - u_{i-1})]\exp\left(-\frac{t_s^{(i)} - t_s^{(i-1)}}{\tau_d}\right)$$

$$u_i = U + [\,u_{i-1} + f(1 - u_{i-1}) + U]\exp\left(-\frac{t_s^{(i)} - t_s^{(i-1)}}{\tau_f}\right)$$

where τ_d and τ_f are the depression and facilitation time-constants. U is the release probability and f is the magnitude of facilitation. To make the estimation more tractable, we approximate the full optimization problem and estimate synaptic delay, t_d, and time-constant, τ_α, by fitting $\alpha(t)$ using the full cross-correlogram, as above. We fix these parameters for the rest of the optimization process. We then maximize a penalized, Bernoulli log-likelihood $l(\theta) = \Sigma\Sigma\left[y_{ij}\lambda_i(t_j) - (1 - y_{ij})\left(1 - \lambda_i(t_j)\right)\right] + \gamma\left\|\theta'_{stp}\right\|_2$ where $\gamma = 1$ is the regularization hyperparameter to estimate the parameters: $\theta = \{\beta_0, \beta_{c=1:C}, \beta_{h=1:H}, A_s, \theta_{stp}\}$, $\theta_{stp} = \{\tau_d, \tau_f, U, f, \tau_s\}$.

As with previous applications of GLMs, we assume that bins are conditionally independent given the covariates, but unlike many other GLMs, here we only calculate the log-likelihood during short intervals (5ms) after presynaptic spikes. With y_{ij} being a binary value representing the presence of a postsynaptic spike in the j-th time bin after the i-th presynaptic spike. We again used a logarithmic transformation for the time-constants to avoid negative values and logit transformation for U and f to bound their values in the interval $[0, 1]$; $\theta'_{stp} = \{\log(\tau_d), \log(\tau_f), \mathrm{logit}(U), \mathrm{logit}(f), \log(\tau_s)\}$. By modeling STP this model is no longer a strict GLM, and the log-likelihood may have local maxima. Here we use random restarts to avoid local maxima in our optimization process. The parameters of each restart $\{\beta_0, \beta_{c=1:C}, \beta_{h=1:H}, A_s\}$ are initialized by adding noise ($\sim N(0,1)$) to the corresponding parameters in a standard GLM. We initialize the plasticity parameters with $\tau'^{(0)}_d \sim N(-1,5)$, $\tau'^{(0)}_f \sim N(-1,5)$, $U'^{(0)} \sim N(0,5)$, $f'^{(0)} \sim N(0,5)$, $\tau'^{(0)}_s \sim N(-3,5)$. We then use an LBFGS algorithm to optimize the log-likelihood where we calculate all derivatives analytically except for derivatives of θ_{stp} which we calculate numerically. To estimate the uncertainty of the parameters, we bootstrap the data from each of the strong synapses by chunking the whole recording time into samples of 50 seconds then resampling the chunks to generate a new spike train with the same original length.

Calculating spike transmission probability

To demonstrate how the probability of postsynaptic spiking changes according to the corresponding presynaptic inter-spike intervals, we estimated spike transmission probabilities from the cross-correlograms directly instead of using a model. To calculate this probability, we focused on a transmission interval after the presynaptic spike where the conditional intensity (when corrected for the baseline rate) goes above 10% of the maximum of $\boldsymbol{\alpha}(t)$. We split the presynaptic inter-spike interval distribution into log-spaced intervals, and, for each interval, we calculate the ratio between numbers of postsynaptic spikes in the transmission interval to the number of presynaptic spikes. Unlike previous studies [14,61] we do not correct this probability for the baseline postsynaptic rate. The uncorrected probability allows us to more directly compare the model predictions to the empirical spike transmission probabilities. Since our model gives an estimate of the postsynaptic probability after each individual presynaptic spike, we can average over the same transmission interval. However, we know if there is a postsynaptic spike in the

transmission interval, probability of a postsynaptic spike goes to ~0 for all consecutive bins due to the post-spike dynamics (e.g. refractory period). Therefore, we measure the predicted probability of a postsynaptic spike in a 5ms window after i-th presynaptic spike from binned $\lambda_i(t_j)$ as follows: $z_i = \sum_{j=1}^{L} \lambda_i(t_j) \prod_{m=1}^{j-1} (1 - \lambda_i(t_m))$. Here we assume conditional independence of the j-th bin after a presynaptic spike, but we enforce a refractory period for all bins after a postsynaptic spike in our generative model. Here L is the first bin that y_{ij} is nonzero. z_i represents the probability of postsynaptic spiking after each presynaptic spike and we fit a smooth curve over the distribution of $z_i{}'$s and their corresponding inter-spike intervals to compare with the empirical spike probability patterns.

Modeling the effect of local patterns of pre- and postsynaptic spiking

The observed and modeled spike transmission patterns, as calculated above, reflect the expected postsynaptic spike probability given a specific presynaptic ISI. However, since the presynaptic ISIs are not independent and there are serial correlations in ISIs, the detailed sequence of the pre- and postsynaptic spiking likely affects the shapes of these curves. To quantify the effects of serial ISI correlations on the model of spike transmission probability we demonstrate how local patterns of presynaptic spiking modifies spike transmission patterns in the data and the model. For each of the three strong identified synapses we measure postsynaptic spiking probability in response to presynaptic spike triplets. Due to the limited number of spikes in our data, we divide the presynaptic ISI distribution into few log-spaced intervals and measure the postsynaptic spiking probability for triplets with the two ISIs that fall in those intervals. Similarly, we measure the predicted postsynaptic probability in response to the presynaptic triplets. After measuring postsynaptic responses to presynaptic spike triplets in the data and the model, we simulate the contribution of STP in shaping the transmission pattern in response to these triplets. To factor out contributions of the postsynaptic history and slow changes in presynaptic firing rate, we fix the corresponding values in the model to their average values within the model. In these simulations, we also fix the initial values of the STP dynamics in the TM model for the first spike of the triplets to the average R and u within the model. This approach enables us to illustrate how short-term synaptic plasticity in triplets of presynaptic spikes changes spike transmission probability and how serial correlations in presynaptic spiking affect spike transmission probability.

The postsynaptic spike history and the serial correlations between the pre- and postsynaptic spiking also modify spike transmission probability patterns. To investigate history effects in the local pattern of pre- and postsynaptic spikes, we measured the postsynaptic spiking probability in response to two presynaptic spikes and a postsynaptic spike preceding the most recent presynaptic spike. Due to the limited number of spikes and sparseness of the split cross-correlograms, we again divided the presynaptic and postsynaptic ISI distributions into a few log-spaced intervals. We then measure the spike transmission probability for a group of presynaptic spikes that their preceding presynaptic ISIs and postsynaptic spike ISIs fall into different combinations of pre- and postsynaptic log-spaced intervals. After measuring postsynaptic responses to any possible

combination of the two most recent presynaptic spikes and their postsynaptic spikes in the data and the model, we simulate the contribution of the history and STP together in shaping the transmission. In our simulation the excitability was set to the model estimates. To measure the effects of postsynaptic spiking history, for each postsynaptic ISI, we fix the history contribution to estimated post-spike history filter value at that postsynaptic ISI. We then use the predicted STP parameters from the data to simulate the STP contribution in response to paired pulses of presynaptic ISIs where we again fix the initial values of the TM model for the first presynaptic spike to the average R and u within the model. This approach enables us to illustrate how short-term synaptic plasticity in local patterns of two presynaptic spikes and a postsynaptic spike changes spike transmission probability and quantifies how serial correlations between pre- and postsynaptic spiking affect spike transmission probability.

Evaluating prediction accuracy

In addition to evaluating the estimated parameters and comparing the model to empirical spike transmission probabilities, we also assess how accurately the model can predict postsynaptic spiking. Not only can we predict the probability of a spike given specific presynaptic ISIs, but we can also predict whether there will be a postsynaptic spike following each individual presynaptic spike. To quantify how well the predicted postsynaptic spike probability, z_i, predicts the postsynaptic spiking activity, we use Receiver Operating Characteristic (ROC) curves. To compute the ROC curve, we first create a threshold version of z_i which operates as our prediction: $\{(\hat{r}_i = 1)$ if $(z_i > \text{thr})$; 0 otherwise$\}$. Changing the threshold from 0 to 1 traces out a relationship between the true positive rate (TPR) and false positive rate (FPR). The area under the ROC curve (AUC) reflects the performance of each model, where a perfect classifier has AUC=1 and a random classifier has AUC=0.5. Effectively, the AUC is the probability of a randomly chosen spike having a higher model probability than a randomly chosen non-spike [72]. Here we calculate the AUC for short intervals (~5ms) after presynaptic spikes and check whether we detect a postsynaptic spike in the transmission interval where $\alpha(t)$ is above 10% of its maximum. Here we compare the AUC for the static model of connectivity without short-term synaptic plasticity with our dynamical model.

A simplified rate model to simulate effects of synaptic summation and post-spike history

Our TM-GLM's prediction of the spike transmission pattern is data-driven and depends on the full history of pre- and postsynaptic spiking. To better understand and illustrate how STP, synaptic summation, and post-spike history interact to create the observed patterns of spike transmission, we simulated postsynaptic responses in a simplified voltage model. Namely, we consider PSP summation in response to a pattern of two presynaptic spikes. We assume that the synapse is initially fully recovered, and the PSC amplitudes are determined by the 4-paramter TM model with $U = 0.7$, $\tau_d = 1.7$, $\tau_f = 0.02$, f =0.05 for the depressing synapse and U =0.1, $\tau_d = 0.02$, $\tau_f = 1$, f =0.11 for the facilitating synapse [28]. We then convolve the PSCs (delta function kernel) with a PSP kernel, $\exp(-t/\tau_v) - \exp(-t/\tau_r)$, with $\tau_v = .01$ and τ_r=.001 ms to describe synaptic

summation. We assume that the instantaneous postsynaptic spike probability is simply a nonlinear function of the distance to a threshold voltage $\sigma\big(5(V(t) - V_{th})\big)$ where $\sigma(x) = 1/(1 + e^{-x})$ and $V_{th} = .5$, $.75$, and 1 correspond to strong, moderate, and weak inputs respectively. The spike transmission probability sums this instantaneous probability over a window of 20ms after each presynaptic spike. Finally, we adjust the spike transmission probability for the second PSP to account for potential post-spike history effects. Namely, we assume that the adjusted spike transmission probability for the second spike is $p_2^* = (1 - p_1)p_2 + p_1 p_2 f_{ahp}$ where p_1 is the transmission probability for the first spike, p_2 is the unadjusted probability for the second spike, and f_{ahp} is the effect of the after-hyperpolarization. Here we use $f_{ahp}(\Delta t) = (\sigma\big(150(\Delta t - 0.02)\big) - c)/d$ where Δt is the presynaptic ISI, and c and d are constants ensuring that $f_{ahp}(0) = 0$ and $f_{ahp}(\infty) = 1$. Although this simulation is highly simplified, it demonstrates how the observed spike transmission pattern depends, not just on the type and timescale of STP, but on the interaction between STP, synaptic summation, after-hyperpolarization effects, and the spike nonlinearity.

Acknowledgements

Thanks to Nick Steinmetz for providing MEA dataset. AG, NR, and IHS were supported by NSF CAREER 1651396 to IHS.

References

1. Abbott LF, Nelson SB. Synaptic plasticity: taming the beast. Nat Neurosci. 2000;3: 1178–1183. doi:10.1038/81453

2. Abbott LF, Regehr WG. Synaptic computation. Nature. 2004. doi:10.1038/nature03010

3. Zucker RS, Regehr WG. Short-term synaptic plasticity. Annu Rev Physiol. 2002;64: 355–405. doi:DOI 10.1146/annurev.physiol.64.092501.114547

4. Regehr WG. Short-term presynaptic plasticity. Cold Spring Harb Perspect Biol. 2012; doi:10.1101/cshperspect.a005702

5. Thomson AM, Lamy C. Functional maps of neocortical local circuitry. Front Neurosci. Frontiers; 2007;1: 19–42. doi:10.3389/neuro.01.1.1.002.2007

6. Dittman JS, Kreitzer AC, Regehr WG. Interplay between facilitation, depression, and residual calcium at three presynaptic terminals. J Neurosci. 2000; doi:10.1523/JNEUROSCI.20-04-01374.2000

7. Wang Y, Markram H, Goodman PH, Berger TK, Ma J, Goldman-Rakic PS. Heterogeneity in the pyramidal network of the medial prefrontal cortex. Nat Neurosci. 2006;9: 534–542. doi:10.1038/nn1670

8. Fortune ES, Rose GJ. Short-term synaptic plasticity as a temporal filter. Trends Neurosci. 2001;24: 381–385. doi:10.1016/S0166-2236(00)01835-X

9. Cook DL, Schwindt PC, Grande LA, Spain WJ. Synaptic depression in the localization of sound. Nature. 2003;421: 66–70. doi:10.1038/nature01248

10. Mongillo G, Barak O, Tsodyks M. Synaptic theory of working memory. Science. 2008;319: 1543–1546. doi:10.1126/science.1150769

11. Abbott LF. Synaptic Depression and Cortical Gain Control. Science (80-). 1997;275: 221–224. doi:10.1126/science.275.5297.221

12. Lindner B, Gangloff D, Longtin A, Lewis JE. Broadband Coding with Dynamic Synapses. J Neurosci. 2009;29: 2076–2087. doi:10.1523/JNEUROSCI.3702-08.2009

13. Drew PJ, Abbott LF. Extending the effects of spike-timing-dependent plasticity to behavioral timescales. Proc Natl Acad Sci. 2006;103: 8876–8881. doi:10.1073/pnas.0600676103

14. Swadlow HA, Gusev AG. The impact of "bursting" thalamic impulses at a neocortical synapse. Nat Neurosci. 2001;4: 402–8. doi:10.1038/86054

15. Usrey WM, Reppas JB, Reid RC. Paired-spike interactions and synaptic efficacy of retinal inputs to the thalamus. Nature. 1998; doi:10.1038/26487

16. English DF, McKenzie S, Evans T, Kim K, Yoon E, Buzsáki G. Pyramidal Cell-Interneuron Circuit Architecture and Dynamics in Hippocampal Networks. Neuron. 2017;96: 505–520. doi:10.1016/j.neuron.2017.09.033

17. Perkel DH, Gerstein GL, Moore GP. Neuronal spike trains and stochastic point processes. II. Simultaneous spike trains. Biophys J. 1967;7: 419–440. Available: http://www.ncbi.nlm.nih.gov/pmc/articles/PMC1368069/

18. Barthó P, Hirase H, Monconduit L, Zugaro M, Harris KD, Buzsáki G. Characterization of Neocortical Principal Cells and Interneurons by Network Interactions and Extracellular Features. J Neurophysiol. 2004;92: 600–608. doi:10.1152/jn.01170.2003

19. Csicsvari J, Hirase H, Czurko A, Buzsáki G. Reliability and state dependence of pyramidal cell-interneuron synapses in the hippocampus: An ensemble approach in the behaving rat. Neuron. 1998;21: 179–189. doi:10.1016/S0896-6273(00)80525-5

20. Fujisawa S, Amarasingham A, Harrison MT, Buzsáki G. Behavior-dependent short-term assembly dynamics in the medial prefrontal cortex. Nat Neurosci. 2008;11: 823–833. doi:10.1038/nn.2134

21. Usrey WM, Alonso JM, Reid RC. Synaptic interactions between thalamic inputs to simple cells in cat visual cortex. J Neurosci. 2000;20: 5461–5467. doi:20/14/5461 [pii]

22. Carandini M, Horton JC, Sincich LC. Thalamic filtering of retinal spike trains by postsynaptic summation. J Vis. 2007;7: 20. doi:10.1167/7.14.20

23. Trussell LO, Zhang S, Ramant IM. Desensitization of AMPA receptors upon multiquantal neurotransmitter release. Neuron. 1993;10: 1185–1196. doi:10.1016/0896-6273(93)90066-Z

24. Henze DA, Buzsáki G. Action potential threshold of hippocampal pyramidal cells in vivo is increased by recent spiking activity. Neuroscience. 2001;105: 121–130. doi:10.1016/S0306-4522(01)00167-1

25. Truccolo W, Eden UT, Fellows MR, Donoghue JP, Brown EN, John P. A Point Process Framework for Relating Neural Spiking Activity to Spiking History, Neural Ensemble, and Extrinsic Covariate Effects. J Neurophysiol. 2005;93: 1074–1089. doi:10.1152/jn.00697.2004

26. Pillow JW, Shlens J, Paninski L, Sher A, Litke AM, Chichilnisky EJ, et al. Spatio-temporal correlations and visual signalling in a complete neuronal population. Nature. Macmillan Publishers Limited. All rights reserved; 2008;454: 995–9. doi:10.1038/nature07140

27. Harris K, Csicsvari J, Hirase H, Dragoi G, Buzsáki G. Organization of cell assemblies in the hippocampus. Nature. 2003;424: 552–556. doi:10.1038/nature01765.1.

28. Ghanbari A, Malyshev A, Volgushev M, Stevenson IH. Estimating short-term synaptic plasticity from pre- and postsynaptic spiking. PLoS Comput Biol. 2017; doi:10.1371/journal.pcbi.1005738

29. Stoelzel CR, Bereshpolova Y, Gusev AG, Swadlow HA. The Impact of an LGNd Impulse on the Awake Visual Cortex: Synaptic Dynamics and the Sustained/Transient Distinction. J Neurosci. 2008; doi:10.1523/JNEUROSCI.4726-07.2008

30. Stoelzel CR, Bereshpolova Y, Swadlow HA. Stability of Thalamocortical Synaptic Transmission across Awake Brain States. J Neurosci. 2009; doi:10.1523/JNEUROSCI.5983-08.2009

31. Thomson AM, West DC, Wang Y, Bannister AP. Synaptic Connections and Small Circuits Involving Excitatory and Inhibitory Neurons in Layers 2-5 of Adult Rat and Cat Neocortex: Triple Intracellular Recordings and Biocytin Labelling In Vitro. Cereb Cortex. Oxford University Press; 2002;12: 936–953. doi:10.1093/cercor/12.9.936

32. Yang H, Xu-Friedman MA. Impact of Synaptic Depression on Spike Timing at the Endbulb of Held. J Neurophysiol. 2009; doi:10.1152/jn.00072.2009

33. Yang H, Xu-Friedman MA. Relative Roles of Different Mechanisms of Depression at the Mouse Endbulb of Held. J Neurophysiol. 2008; doi:10.1152/jn.01293.2007

34. Gerhard F, Kispersky T, Gutierrez GJ, Marder E, Kramer M, Eden U. Successful Reconstruction of a Physiological Circuit with Known Connectivity from Spiking Activity Alone. PLoS Comput Biol. 2013;9. doi:10.1371/journal.pcbi.1003138

35. Stevenson IH, London BM, Oby ER, Sachs NA, Reimer J, Englitz B, et al. Functional Connectivity and Tuning Curves in Populations of Simultaneously Recorded Neurons. PLoS Comput Biol. Public Library of Science; 2012;8: e1002775. doi:10.1371/journal.pcbi.1002775

36. Markram H, Wang Y, Tsodyks M. Differential signaling via the same axon of neocortical pyramidal neurons. Proc Natl Acad Sci U S A. 1998;95: 5323–8. doi:10.1073/pnas.95.9.5323

37. Huang C, Resnik A, Celikel T, Englitz B. Adaptive Spike Threshold Enables Robust and Temporally Precise Neuronal Encoding. PLoS Comput Biol. 2016; doi:10.1371/journal.pcbi.1004984

38. Costa RP, Sjöström PJ, van Rossum MCW. Probabilistic inference of short-term synaptic plasticity in neocortical microcircuits. Front Comput Neurosci. 2013;7: 75. doi:10.3389/fncom.2013.00075

39. Gil Z, Connors BW, Amitai Y. Differential regulation of neocortical synapses by neuromodulators and activity. Neuron. 1997; doi:10.1016/S0896-6273(00)80380-3

40. Wang Y, Manis PB. Synaptic Transmission at the Cochlear Nucleus Endbulb Synapse During Age-Related Hearing Loss in Mice. J Neurophysiol. 2005; doi:10.1152/jn.00374.2005

41. Wang Y, Manis PB. Short-term synaptic depression and recovery at the mature mammalian endbulb of Held synapse in mice. J Neurophysiol. 2008; doi:10.1152/jn.90715.2008

42. Paz JT, Chavez M, Saillet S, Deniau J-M, Charpier S. Activity of Ventral Medial Thalamic Neurons during Absence Seizures and Modulation of Cortical Paroxysms by the Nigrothalamic Pathway. J Neurosci. 2007; doi:10.1523/JNEUROSCI.4677-06.2007

43. Moore AK, Wehr M. Parvalbumin-Expressing Inhibitory Interneurons in Auditory Cortex Are Well-Tuned for Frequency. J Neurosci. 2013;33: 13713–13723. doi:10.1523/JNEUROSCI.0663-13.2013

44. Perrenoud Q, Rossier J, Geoffroy H, Vitalis T, Gallopin T. Diversity of gabaergic interneurons in layer VIa and VIb of mouse barrel cortex. Cereb Cortex. 2013; doi:10.1093/cercor/bhs032

45. Harris K, Csicsvari J, Hirase H, Dragoi G, Buzsáki G. Organization of cell assemblies in the hippocampus. Nature. 2003;424: 552–556. doi:10.1038/nature01765.1.

46. Moore GP, Segundo JP, Perkel DH, Levitan H. Statistical Signs of Synaptic Interaction in Neurons. Biophys J. 1970;10: 876–900. doi:10.1016/S0006-3495(70)86341-X

47. London M, Schreibman A, Haä;usser M, Larkum ME, Segev I. The information efficacy of a synapse. Nat Neurosci. 2002;5: 332–340. doi:10.1038/nn826

48. Pinault D. The juxtacellular recording-labeling technique. Neuromethods. 2011. doi:10.1007/978-1-60327-202-5_3

49. Weiler N, Wood L, Yu J, Solla SA, Shepherd GMG. Top-down laminar organization of the excitatory network in motor cortex. Nat Neurosci. 2008; doi:10.1038/nn2049

50. Ladenbauer J, McKenzie S, English DF, Hagens O, Ostojic S. Inferring and validating mechanistic models of neural microcircuits based on spike-train data. bioRxiv Prepr. 2018; doi:10.1101/261016

51. McFarland JM, Cui Y, Butts DA. Inferring Nonlinear Neuronal Computation Based on Physiologically Plausible Inputs. PLoS Comput Biol. 2013;9. doi:10.1371/journal.pcbi.1003143

52. Robinson BS, Berger TW, Song D. Identification of stable spike-timing-dependent plasticity from spiking activity with generalized multilinear modeling. Neural Comput. 2016; doi:10.1162/NECO_a_00883

53. Song D, Robinson BS, Berger TW. Identification of Short-Term and Long-Term Functional Synaptic Plasticity From Spiking Activities. Adaptive Learning Methods for Nonlinear System Modeling. Elsevier; 2018. pp. 289–312. doi:10.1016/B978-0-12-812976-0.00017-8

54. Stevenson I, Koerding K. Inferring spike-timing-dependent plasticity from spike train data. Adv Neural Inf Process Syst. 2011; 1–9. Available: http://machinelearning.wustl.edu/mlpapers/paper_files/NIPS2011_1399.pdf

55. Linderman S, Stock C, Adams R. A framework for studying synaptic plasticity with neural spike train data. Adv Neural Inf. 2014; Available: http://arxiv.org/abs/1411.4077

56. Amidi Y, Nazari B, Sadri S, … UE-2018 40th A, 2018 U. Parameter Estimation in Synaptic Coupling Model Using a Point Process Modeling Framework*. ieeexplore.ieee.org. 2018; doi:10.1109/EMBC.2018.8512815

57. Bayat Mokhtari E, Lawrence JJ, Stone EF. Data Driven Models of Short-Term Synaptic Plasticity. Front Comput Neurosci. 2018; doi:10.3389/fncom.2018.00032

58. Markram H, Muller E, Ramaswamy S, Reimann MW, Abdellah M, Sanchez CA, et al. Reconstruction and Simulation of Neocortical Microcircuitry. Cell. 2015;163: 456–492. doi:10.1016/j.cell.2015.09.029

59. Karmarkar UR, Buonomano D V. Timing in the Absence of Clocks: Encoding Time in Neural Network States. Neuron. 2007; doi:10.1016/j.neuron.2007.01.006

60. Klyachko VA, Stevens CF. Excitatory and feed-forward inhibitory hippocampal synapses work synergistically as an adaptive filter of natural spike trains. PLoS Biol. 2006;4: 1187–1200. doi:10.1371/journal.pbio.0040207

61. Swadlow HA, Gusev AG. Receptive-field construction in cortical inhibitory interneurons. Nature Neuroscience. 2002. doi:10.1038/nn847

62. Kawaguchi Y. Distinct firing patterns of neuronal subtypes in cortical synchronized activities. J Neurosci. 2001; doi:21/18/7261 [pii]

63. Swadlow HA. Thalamocortical control of feed-forward inhibition in awake somatosensory "barrel" cortex. Philos Trans R Soc Lond B Biol Sci. 2002;357: 1717–27. doi:10.1098/rstb.2002.1156

64. Keine C, Rübsamen R, Englitz B. Signal integration at spherical bushy cells enhances representation of temporal structure but limits its range. Elife. 2017;6. doi:10.7554/eLife.29639

65. Keine C, Rubsamen R, Englitz B. Inhibition in the auditory brainstem enhances signal representation and regulates gain in complex acoustic environments. Elife. 2016;5. doi:10.7554/eLife.19295

66. Mora Lopez C, Putzeys J, Raducanu BC, Ballini M, Wang S, Andrei A, et al. A Neural Probe with Up to 966 Electrodes and Up to 384 Configurable Channels in 0.13 µm SOI CMOS. IEEE Trans Biomed Circuits Syst. 2017;11: 510–522. doi:10.1109/TBCAS.2016.2646901

67. Jun JJ, Steinmetz NA, Siegle JH, Denman DJ, Bauza M, Barbarits B, et al. Fully integrated silicon probes for high-density recording of neural activity. Nature. 2017;551: 232–236. doi:10.1038/nature24636

68. Pachitariu M, Steinmetz N, Kadir S, Carandini M, Harris KD. Kilosort: realtime spike-sorting for extracellular electrophysiology with hundreds of channels [Internet]. bioRxiv. 2016. doi:10.1101/061481

69. Dale H. Pharmacology and Nerve-endings. J R Soc Med. 1935;28: 319–332. doi:10.1177/003591573502800330

70. Tsodyks M, Pawelzik K, Markram H. Neural networks with dynamic synapses. Neural Comput 1998 May;10(4)821-835. 1998;835: 821–835. doi:10.1162/089976698300017502

71. Tsodyks M V., Markram H. The neural code between neocortical pyramidal neurons depends on neurotransmitter release probability. Proc Natl Acad Sci. 1997;94: 719–723. doi:10.1073/pnas.94.2.719

72. Hatsopoulos NG, Xu Q, Amit Y. Encoding of Movement Fragments in the Motor Cortex. J Neurosci. 2007;27: 5105–5114. doi:10.1523/JNEUROSCI.3570-06.2007

Figure 6— figure supplement 1: Spike transmission probabilities patterns and cross-correlograms for each of the microcircuits identified from the multi-electrode array recording. Excitatory inputs (cross-correlograms at left with corresponding transmission probability (Prob.) numbers) to the putative inhibitory neurons are shown along with selected outgoing cross-correlograms used to identify putative inhibitory neurons (right). Spike wave-shapes are shown in each circle. Top panel shows the disentangled paired-pulse ratios using simulations following model fits – membrane integration (yellow); STP (blue); integration and STP (orange). Numbers on each line connecting putative excitatory neurons and the inhibitory neuron corresponds to depth differences between recording electrodes.

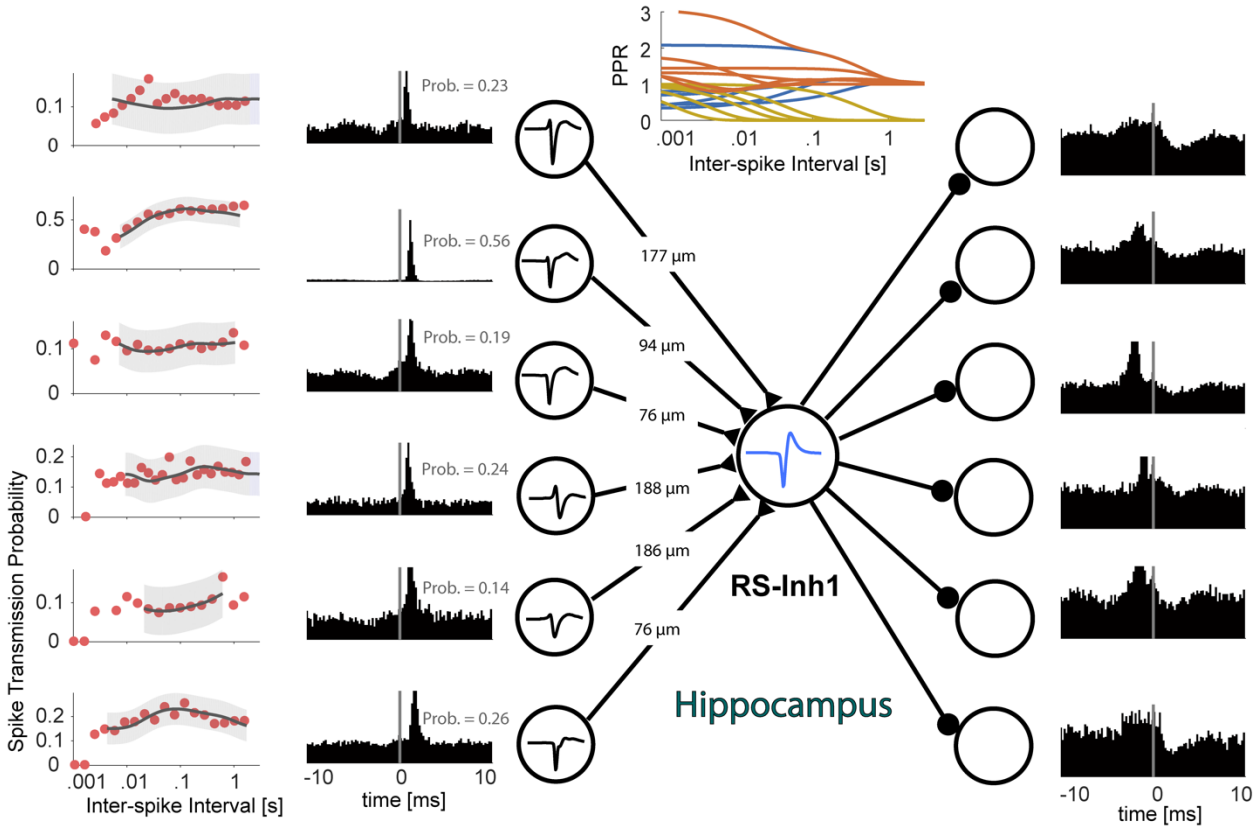

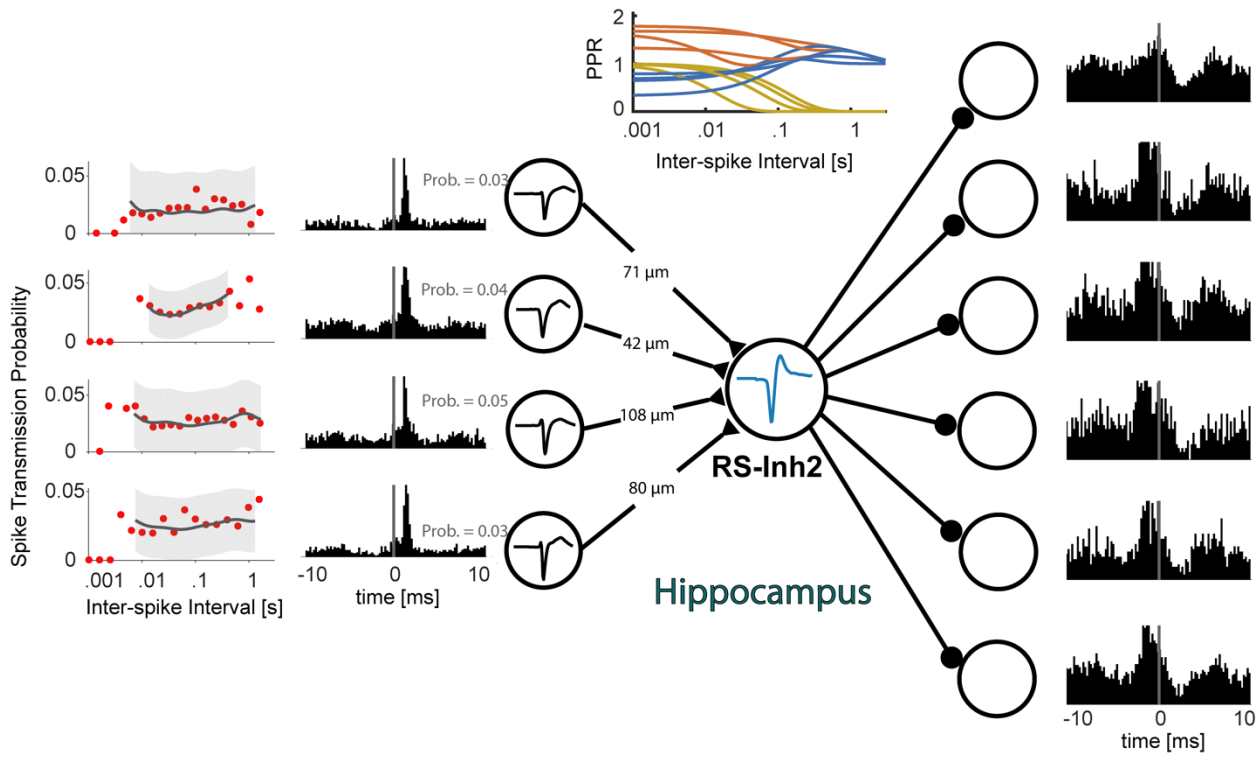
PPR
Inter-spike Interval [s]
Spike Transmission Probability
Inter-spike Interval [s]
time [ms]
Prob. = 0.03
Prob. = 0.04
Prob. = 0.05
Prob. = 0.03
71 µm
42 µm
108 µm
80 µm
RS-Inh2
Hippocampus
time [ms]

1073

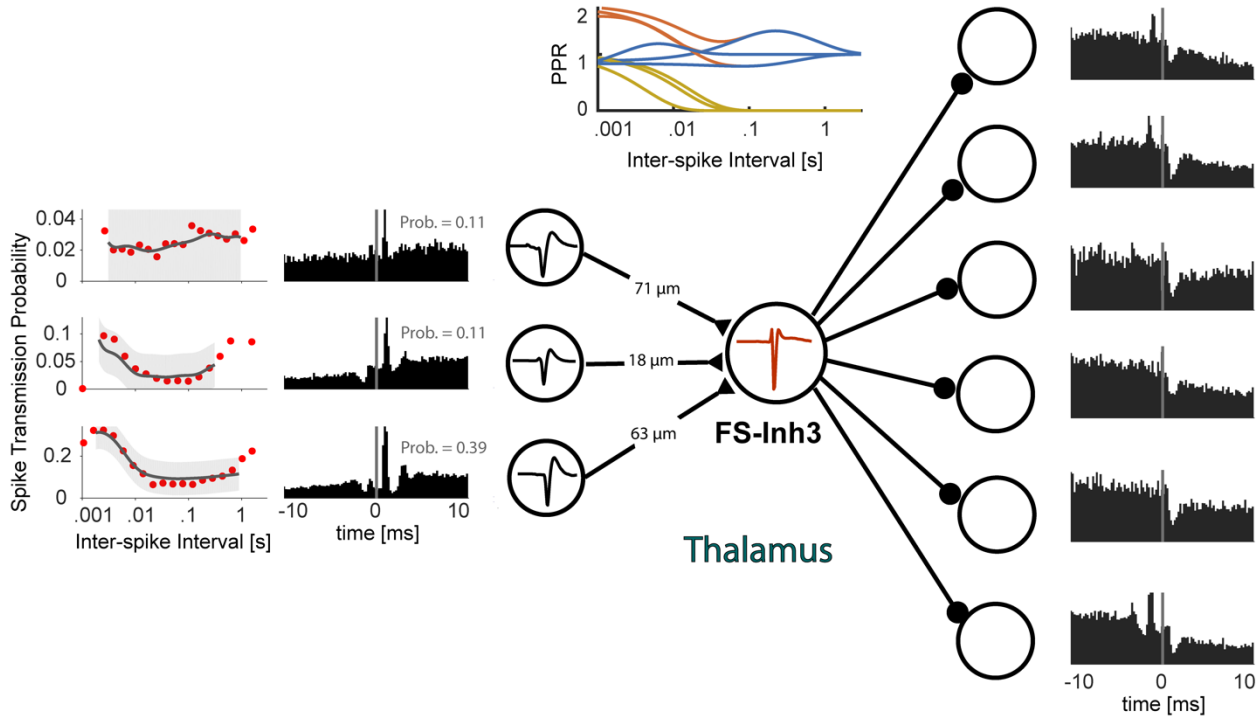
PPR
Inter-spike Interval [s]
Spike Transmission Probability
Inter-spike Interval [s]
time [ms]
Prob. = 0.11
Prob. = 0.11
Prob. = 0.39
71 µm
18 µm
63 µm
FS-Inh3
Thalamus
time [ms]

1074

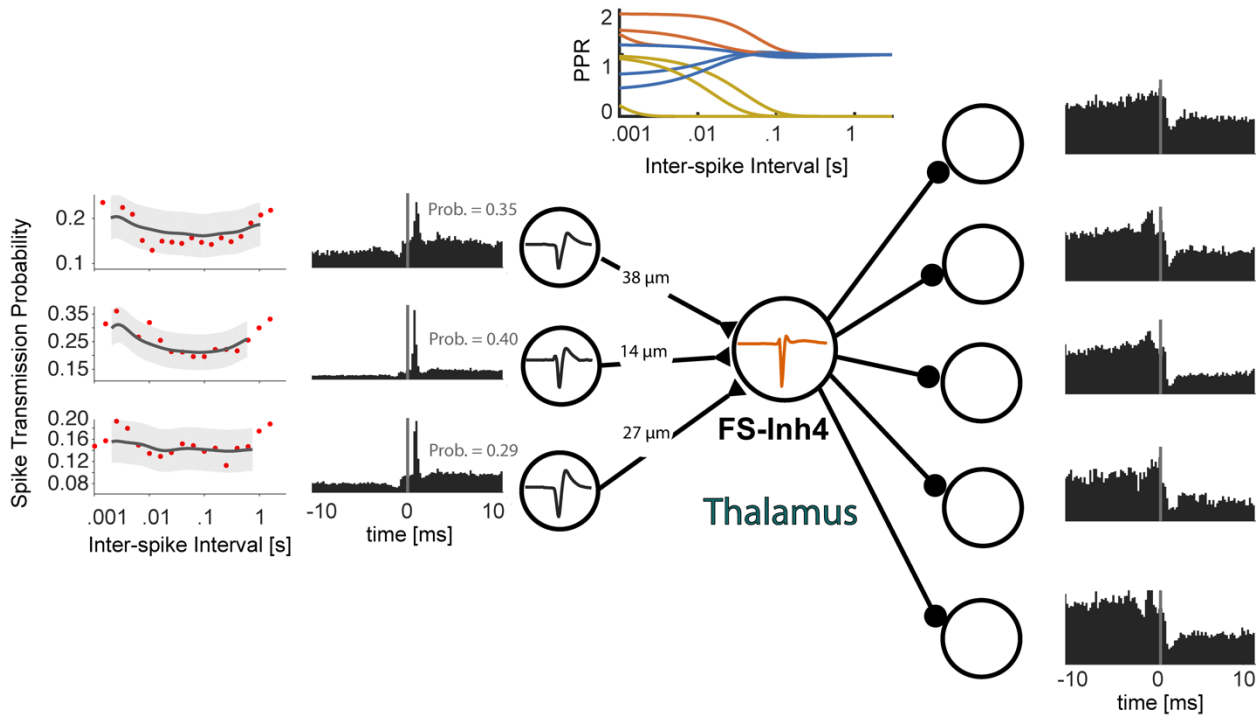
PPR
Inter-spike Interval [s]
Spike Transmission Probability
Prob. = 0.35
Prob. = 0.40
Prob. = 0.29
38 µm
14 µm
27 µm
FS-Inh4
Thalamus
time [ms]

1075

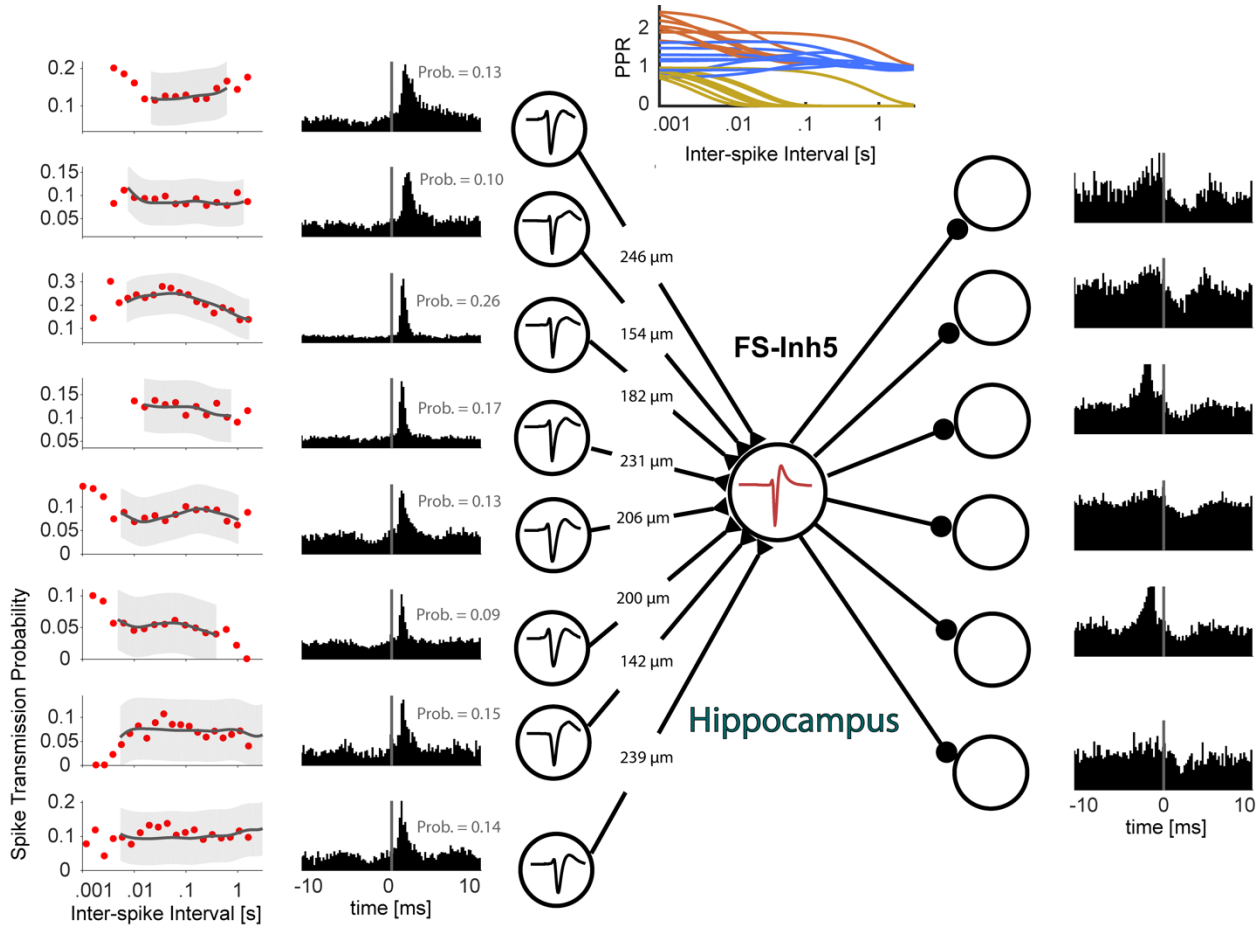
PPR
Inter-spike Interval [s]
Spike Transmission Probability
Prob. = 0.13
Prob. = 0.10
Prob. = 0.26
Prob. = 0.17
Prob. = 0.13
Prob. = 0.09
Prob. = 0.15
Prob. = 0.14
246 µm
154 µm
182 µm
231 µm
206 µm
200 µm
142 µm
239 µm
FS-Inh5
Hippocampus
time [ms]

1076

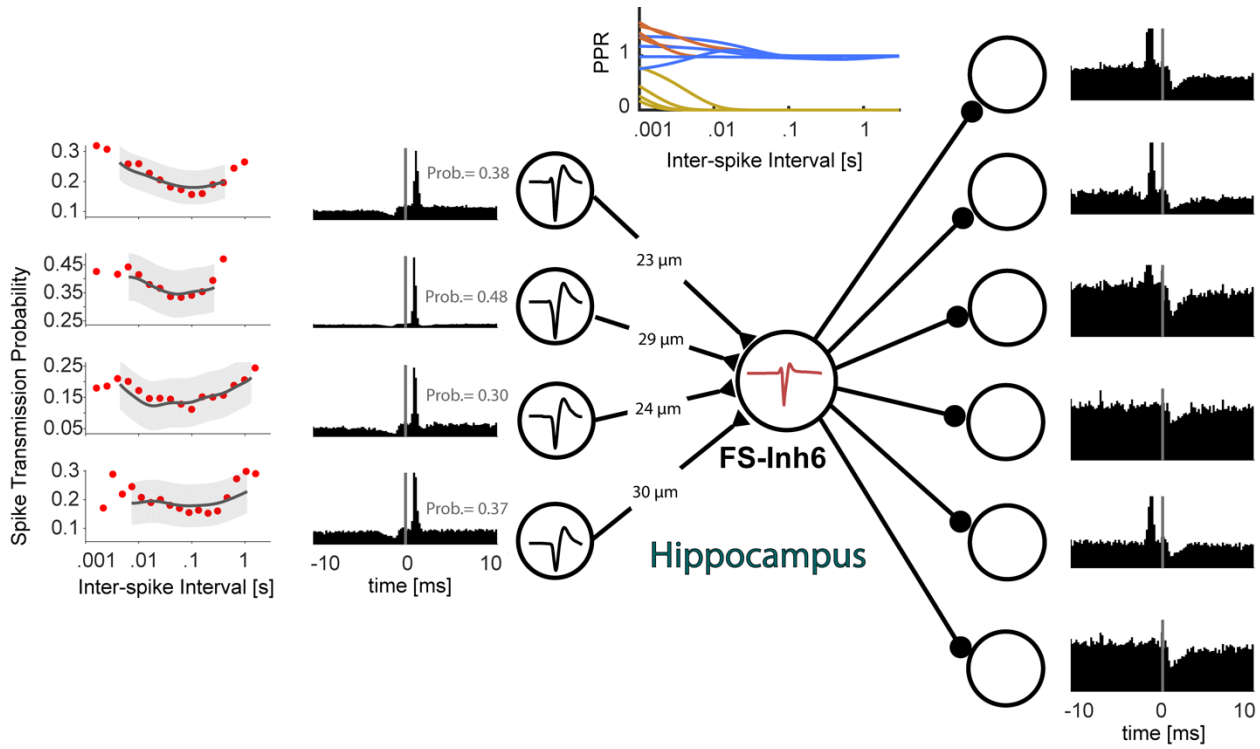
PPR
Inter-spike Interval [s]
Spike Transmission Probability
Inter-spike Interval [s]
Prob.= 0.38
Prob.= 0.48
Prob.= 0.30
Prob.= 0.37
time [ms]
23 µm
29 µm
24 µm
30 µm
FS-Inh6
Hippocampus
time [ms]

1077

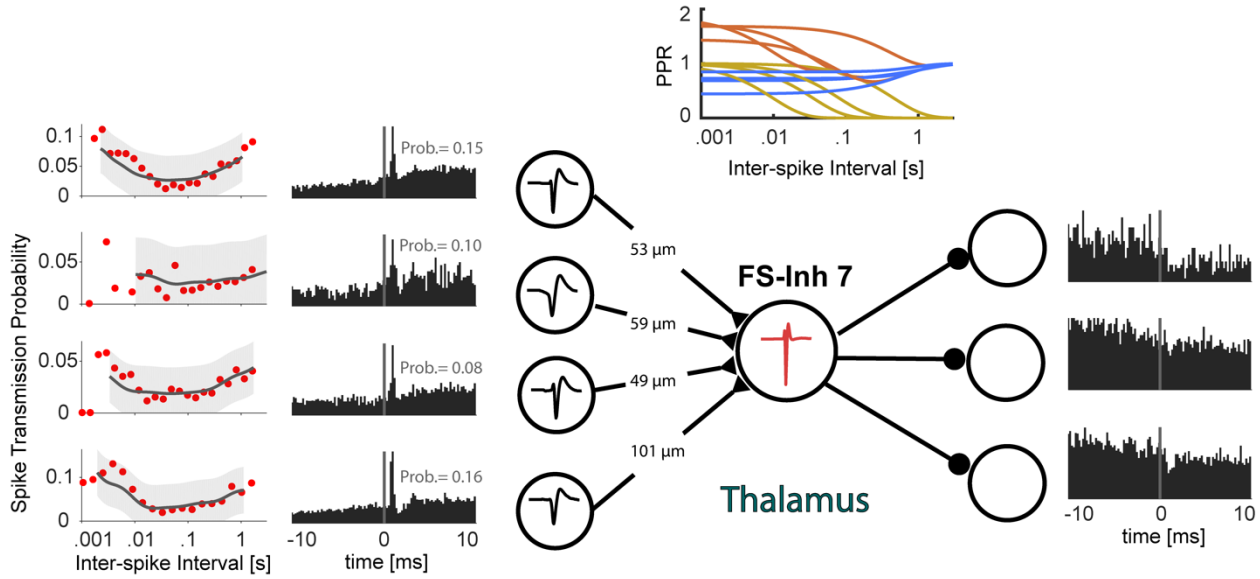
PPR
Inter-spike Interval [s]
Spike Transmission Probability
Inter-spike Interval [s]
Prob.= 0.15
Prob.= 0.10
Prob.= 0.08
Prob.= 0.16
time [ms]
53 µm
59 µm
49 µm
101 µm
FS-Inh 7
Thalamus
time [ms]

1078

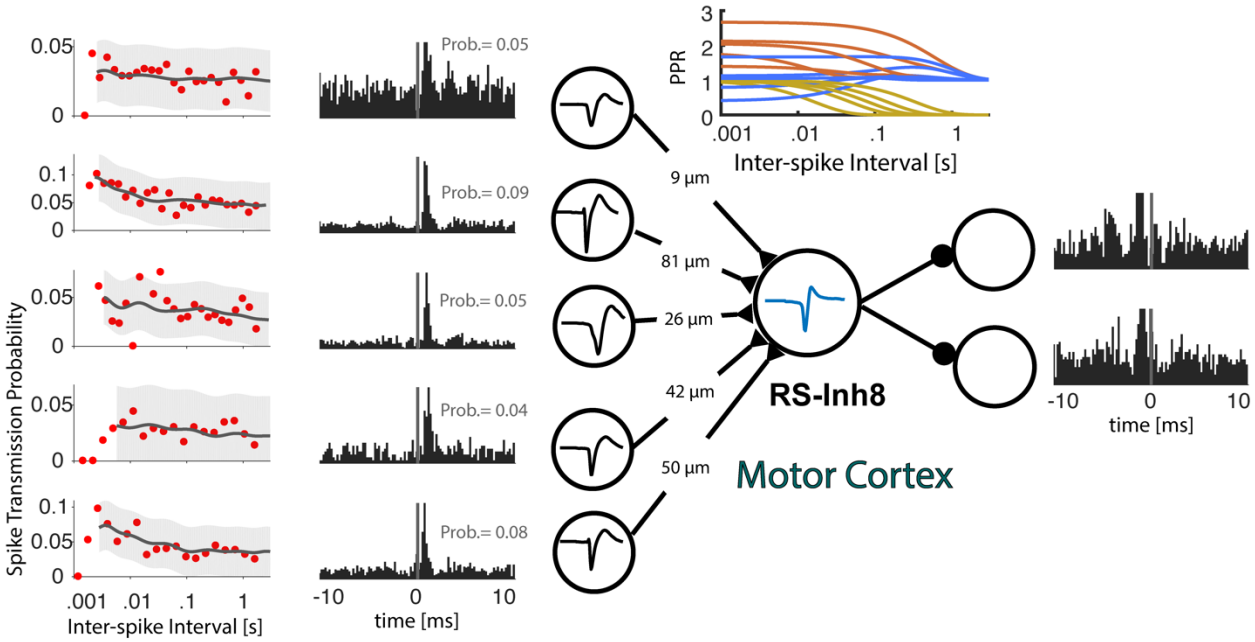
Spike Transmission Probability
Inter-spike Interval [s]
Prob.= 0.05
Prob.= 0.09
Prob.= 0.05
Prob.= 0.04
Prob.= 0.08
time [ms]
PPR
Inter-spike Interval [s]
9 µm
81 µm
26 µm
42 µm
50 µm
RS-Inh8
Motor Cortex
time [ms]

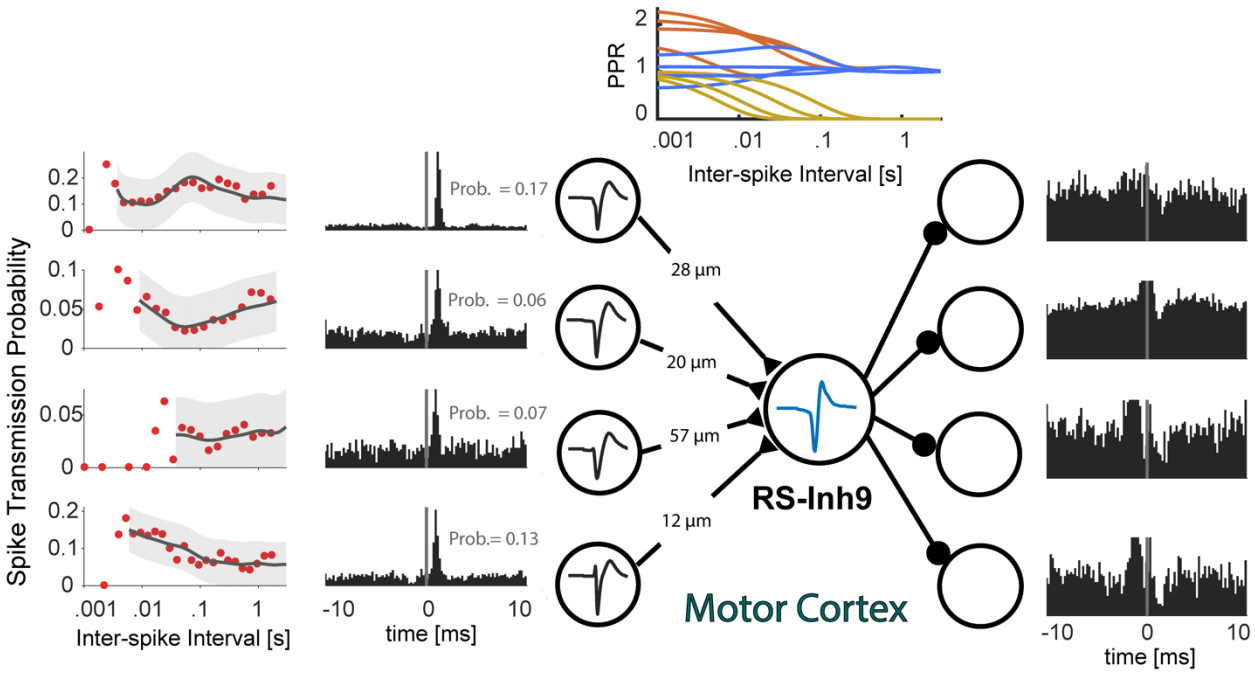
PPR
Inter-spike Interval [s]
Spike Transmission Probability
Inter-spike Interval [s]
Prob. = 0.17
Prob. = 0.06
Prob. = 0.07
Prob.= 0.13
time [ms]
28 µm
20 µm
57 µm
12 µm
RS-Inh9
Motor Cortex
time [ms]